The Astrophysical Journal, 903:74 (22pp), 2020 November 1 https://doi.org/10.3847/1538-4357/abb826

On the Correlation between L Dwarf Optical and Infrared Variability and Radio Aurorae

Tyler Richey-Yowell[1], Melodie M. Kao[1,4], J. Sebastian Pineda[2], Evgenya L. Shkolnik[1], and Gregg Hallinan[3]
[1] School of Earth and Space Exploration, Arizona State University, Tempe, AZ 85281, USA; tricheyy@asu.edu
[2] University of Colorado Boulder, Laboratory for Atmospheric and Space Physics, 3665 Discovery Drive, Boulder, CO 80303, USA
[3] California Institute of Technology, Department of Astronomy, 1200 E. California Avenue, Pasadena, CA 91125, USA
Received 2020 March 25; revised 2020 September 10; accepted 2020 September 10; published 2020 November 3

Abstract

Photometric variability attributed to cloud phenomena is common in L/T transition brown dwarfs. Recent studies show that such variability may also trace aurorae, suggesting that localized magnetic heating may contribute to observed brown dwarf photometric variability. We assess this potential correlation with a survey of 17 photometrically variable brown dwarfs using the Karl G. Jansky Very Large Array at 4–8 GHz. We detect quiescent and highly circularly polarized flaring emission from one source, 2MASS J17502484-0016151, which we attribute to auroral electron cyclotron maser emission. The detected auroral emission extends throughout the frequency band at $\sim$5–25σ, and we do not detect evidence of a cutoff. Our detection confirms that 2MASS J17502484-0016151 hosts a magnetic field strength of $\geqslant$2.9 kG, similar to those of other radio-bright ultracool dwarfs. We show that Hα emission continues to be an accurate tracer of auroral activity in brown dwarfs. Supplementing our study with data from the literature, we calculate the occurrence rates of quiescent emission in L dwarfs with low- and high-amplitude variability and conclude that high-amplitude optical and infrared variability does not trace radio magnetic activity in L dwarfs.

Unified Astronomy Thesaurus concepts: Brown dwarfs (185); L dwarfs (894); Radio astronomy (1338); Radio observatories (1350); Clouds (258); Radio continuum emission (1340); Radio sources (1358)

1. Introduction

Even before the first confirmed discovery of a brown dwarf by Nakajima et al. (1995), theoretical models of brown dwarfs have long been concerned with the interpretation of clouds in their atmospheres (e.g., Lunine et al. 1989). Prior to the development of real cloud treatments, cloudless models were used to trace the brown dwarf spectral sequence. While some studies argue that cloudless models are still applicable (e.g., Tremblin et al. 2015, 2016), many others have argued that clouds are ubiquitous within brown dwarf atmospheres and play a key role in our understanding of the evolution of brown dwarfs as they cool throughout their lifetimes. For instance, the transition between L and T spectral types occurs when iron, silicates, and metal oxide compounds condense and begin raining out of the atmosphere (Allard et al. 2001; Tsuji 2002). The remaining cloud coverage is expected to be patchy, which may be the primary source of photometric variability in the optical and infrared (e.g., Apai et al. 2013; Radigan 2013). Numerous ground- and space-based studies demonstrate that most (>50%) of brown dwarfs exhibit optical and infrared (O/IR) variability (e.g., Radigan 2014; Heinze et al. 2015; Metchev et al. 2015). Such variability can be periodic or irregular (Bailer-Jones & Mundt 2001; Koen 2005; Metchev et al. 2015). Because the atmospheres of brown dwarfs are expected to be neutral from their cool (<2000 K) temperatures, Mohanty et al. (2002) and Radigan (2013) proposed silicate clouds as the source of the observed variability.

In the last decade, the discovery that brown dwarfs emit aurorae underscores the possibility that localized magnetic heating due to the energy deposition from the auroral currents may also play a role in brown dwarf variability. Hallinan et al. (2007) confirmed that brown dwarf radio flares, first detected on LP 944-20 by Berger et al. (2001), are emitted via the electron cyclotron maser instability (ECMI). ECMI is also the source of Jupiter's radio aurorae (Zarka 1992), and Hallinan et al. (2015) argued that a single magnetospheric current could cause the simultaneous periodic optical and radio variability observed from the brown dwarf LSR J1835+3259. Soon thereafter, Kao et al. (2016) demonstrated that tracers of Jovian aurorae such as Hα emission (e.g., Clary & Hunter 1975) and infrared photometric variability (e.g., Caldwell et al. 1980) also appear to be correlated with brown dwarf radio aurorae, further evidence that brown dwarf radio emission was auroral in nature. Finally, Pineda et al. (2017) showed that brown dwarf radio and Hα luminosities are correlated. This suggested that, despite the lack of global coronal heating indicated by the sharp drop-off in X-ray luminosities for brown dwarfs (Williams et al. 2014), radio and Hα emission from brown dwarfs trace the same current systems.

So far though, models interpreting observed photometric variability in L/T transition brown dwarfs do not take into account the role of localized magnetic heating from auroral currents, as this mechanism and other inhomogeneous surface features cannot be reproduced with current 1D cloud models (Biller 2017). However, spectral models of T dwarf atmospheres show that localized atmospheric heating can result in excess flux at at 1–10 μm (Morley et al. 2014). Similarly, Robinson & Marley (2014) show that periodic heating perturbations may produce flux variations on the order of 1%–3% on timescales of both hours and days, including temporal phase shifts of the maximum flux observed at different wavelengths. Thus, thermal influences may additionally contribute to the photometric variability seen on brown dwarfs. Energy deposition from the auroral currents impacting the atmosphere may be one such source of thermal influence.

[4] NASA Hubble Postdoctoral Fellow.

Hallinan et al. (2015) and later Kao et al. (2016) suggested that the inferred non-thermal electron beams traversing the magnetospheres of these brown dwarfs implied by auroral detections could cause spot heating at the base of these electron beams in the upper atmospheres of brown dwarfs. These types of interactions are readily seen in Jupiter's (e.g., Drossart et al. 1989), Saturn's (e.g., Geballe et al. 1993), and Uranus' aurorae (e.g., Trafton et al. 1993). In the case of Jupiter, both models and observations have demonstrated that magnetosphere-ionosphere coupling drive the thermal profile of the atmosphere. Using a fully 3D Jupiter Thermospheric General Circulation Model, Bougher et al. (2005) showed that both moderate auroral particle and Joule heating are necessary to recreate observed temperatures over a range of latitudes above the homopause. Recent observations in the infrared by Sinclair et al. (2019) have demonstrated that the brightness temperatures of Jupiter's poles increase by several kelvin (∼25%) in a matter of days with in an increase in auroral power, in this case due to the solar wind. These observations suggest that the auroral heating on Jupiter may occur even as deep as the upper stratosphere (10–1 μbar).

Targeted searches have shown that there may indeed be a connection between these auroral features and the photometric variability. Harding et al. (2013) observed six objects for which auroral radio emission was detected and found that five displayed infrared variability associated with the radio-measured rotation period of the brown dwarf, with the sixth showing a marginal detection. Hallinan et al. (2015) demonstrated that a single auroral feature can explain optical photometric variability at different bands that is both in and out of phase for the radio aurora emitting M9.5 dwarf LSR J1835+3259. Similarly, Kao et al. (2016) observed six additional late L and T dwarfs known to exhibit Hα emission and/or O/IR variables and found five of six to be auroral radio sources, demonstrating that there may also be a connection from radio emission to Hα emission and/or O/IR variability.

Further characterizing the possible overlap between observational markers of magnetism and clouds on brown dwarfs is imperative for accurately modeling brown dwarf cloud characteristics. We present a search for radio emission indicative of magnetism in a radio survey of 17 brown dwarfs using the the Karl G. Jansky Very Large Array (VLA) from 4–8 GHz (Section 3). Our targets are late L dwarfs in the transition region from L to T spectral types, where cooling temperatures cause clouds to precipitate out and result in patchy cloud coverage with strong O/IR variability amplitudes (0.5%–26%; Section 2). Our target sample allows us to statistically constrain the presence of localized atmospheric heating to observed photometric variability attributed to cloud phenomena (Sections 4 and 5).

2. Targets

We selected our sample of 17 objects to include only those with photometric variability at *I*, *R*, *J*, *H*, and/or *K* bands to test whether this variability can be attributed to a magnetically driven component in addition to cloudy atmospheres. Table 1 presents the target summary. In this work, we chose to focus on L dwarfs; however, in Section 5 we discuss combining this work with independent analysis of T dwarf O/IR variability and radio aurorae to yield a correlation over the full range of the L/T spectral sequence. Below we outline the literature in regards to the photometric variability, previous radio searches, and Hα activity of each of our targets. We additionally include a summary table as Table 2.

2MASSI J0030300-145033. 2M0030-14 was discovered and classified as an L6.5 dwarf by Kirkpatrick et al. (2000) using data from the Two Micron All Sky Survey (2MASS; Skrutskie et al. 2006). Enoch et al. (2003) saw a magnitude change of 0.19 ± 0.11 mag in the *K* band. Other observations in i, z, J, H, and K bands by Koen et al. (2005), Clarke et al. (2008), Schmidt et al. (2015), and Radigan (2014) reported no variability. Berger (2006) placed an upper limit on its radio emission of 57 μJy at 8.46 GHz. Schmidt et al. (2015) placed an upper limit on the Hα activity of 2M0030-14 of $\log(L_{\rm H\alpha}/L_{\rm bol}) < -5.04$.

2MASSI J0103320+193536. 2M0103+19 was discovered by Kirkpatrick et al. (2000) and is classified as an L6 dwarf (Metchev et al. 2015). Metchev et al. (2015) identified a rotation period of 2.7 ± 0.1 hr and saw variability in the Spitzer Infrared Array Camera (IRAC) channels 1 (3.6 μm) and 2 (4.6 μm) with magnitude changes of $0.56 \pm 0.03\%$ and $0.87 \pm 0.09\%$, respectively. Additionally, Enoch et al. (2003) observed *K* band variability of 0.10 ± 0.02 mag and no variability in the *J* band, the latter of which was confirmed by Vos et al. (2019). Schmidt et al. (2015) placed an upper limit on the Hα activity of 2M0103+19 of $\log(L_{\rm H\alpha}/L_{\rm bol}) < -5.96$.

2MASS J01075242+0041563. 2M0107+00 was discovered by Geballe et al. (2002) using data from the Sloan Digital Sky Survey (SDSS; York et al. 2000) and is classified as an L8 dwarf (Schneider et al. 2014). Metchev et al. (2015) observed 2M0107+00 to have an irregular period between 5–13 hr with variability at 3.6 μm and 4.6 μm of $1.27 \pm 0.13\%$ and $1.0 \pm 0.2\%$, respectively. Schmidt et al. (2015) placed an upper limit on the Hα activity of 2M0107+00 of $\log(L_{\rm H\alpha}/L_{\rm bol}) < -4.94$.

2MASSW J0310599+164816. 2M0310+16 was discovered by Kirkpatrick et al. (2000) who classified it as an L8 dwarf. More recently Stumpf et al. (2010) resolved 2M0310+16 as a brown dwarf binary system with a separation of <6 au. Using HST/WFC3 in the IR channel, Buenzli et al. (2014) saw an amplitude change of 2% per hour at 1.26–1.32 μm. Schmidt et al. (2015) placed an upper limit on the Hα activity of 2M0310+16 of $\log(L_{\rm H\alpha}/L_{\rm bol}) < -5.65$.

2MASS J08354256-0819237. 2M0835-08 was identified and classified as an L6.5 dwarf by Salim et al. (2003). It has a known rotation period as seen in the *I* band of 3.1 hr (Koen 2004). Radigan (2014) reported a $1.3 \pm 0.2\%$ amplitude variation in the *J* band, whereas Wilson et al. (2014) reported $1.6 \pm 0.5\%$. Koen (2004) saw a 10 mmag amplitude in the *I* band. No variability is seen in the *R* band (Koen et al. 2005). Schlawin et al. (2017) observed 2M0835-08 with SpeX IRTF J, H, and K broad bands from 0.9 to 2.4 μm and placed an upper limit of <0.5% semi-amplitude in each band. Berger (2006) reported a non-detection searching for radio emission with a sensitivity of 30 μJy. Reiners & Basri (2008) placed an upper limit on the Hα activity of 2M0835-08 to be $\log(L_{\rm H\alpha}/L_{\rm bol}) < -7.42$. More recently, Schmidt et al. (2015) placed the upper limit on the Hα activity at −6.60, which is similar to the upper limit of −6.5 seen by Pineda et al. (2016).

2MASS J10101480-0406499. 2M1010-04 was discovered by and identified as an L6 dwarf by Cruz et al. (2003). Wilson et al. (2014) reported the variability in the *J* band to be $5.1 \pm 1.1\%$; however, the data was reanalyzed independently by Radigan (2014) who found it to be $3.6 \pm 0.4\%$. There have been no Hα observations of 2M1010-04.

Table 1
Target Information for the 17 L Dwarfs in Our Sample

Object Name	Abbrev. Name	SpT	References	Distance (pc)	References	$\mu_\alpha \cos\delta$ (mas yr^{-1})	μ_δ (mas yr^{-1})	References	$\log(L_{H\alpha}/L_{bol})$	References
2MASSI J0030300-145033	2M0030-14	L6.5	1	26.72 ± 3.21	10	245 ± 4	−28 ± 2	13	<−5.04	18
2MASSI J0103320+193536	2M0103+19	L6	2	21.32 ± 3.46	10	305 ± 17	35 ± 14	14	<−5.96	18
2MASS J01075242+0041563	2M0107+00	L8	3	15.59 ± 1.1	10	623 ± 10	91 ± 1	9	<−4.94	18
2MASSW J0310599+164816	2M0310+16	L8	1	27.1 ± 2.5	11	245.9 ± 4	6.2 ± 3.3	11	<−5.65	18
2MASS J08354256-0819237	2M0835-08	L6.5	4	7.21 ± 0.01	12	−535.657 ± 0.439	302.737 ± 0.405	12	<−7.42	19
2MASS J10101480-0406499	2M1010-04	L6	5	16.72 ± 2.27	10	−321 ± 16	20 ± 13	14	⋯	⋯
2MASS J10433508+1213149	2M1043+12	L9	3	14.6 ± 2.26	10	26 ± 5.1	−234.2 ± 3.9	10	⋯	⋯
DENIS-P J1058.7-1548	DENIS 1058-15	L2.5	3	18.3 ± 0.18	12	−258.068 ± 0.809	31.104 ± 0.732	12	−5.59	18
2MASS J12195156+3128497	2M1219+31	L8	6	18.1 ± 3.7	21	−233 ± 23.7	−49.6 ± 14.7	15	⋯	⋯
2MASS J14252798-3650229	2M1425-36	L5	7	11.83 ± 0.05	12	−283.863 ± 0.611	−469.283 ± 0.48	12	<−5.03	18
2MASS J16154255+4953211	2M1615+49	L4γ	8	31.25 ± 0.98	17	−80 ± 12	18 ± 12	16	⋯	⋯
2MASS J16322911+1904407	2M1632+19	L8	3	15.24 ± 0.49	10	293 ± 1	−54 ± 1	13	<−5.52	18
2MASS J17114573+2232044	2M1711+22	L9.5	3	30.2 ± 4.39	10	31 ± 7	−5 ± 4	13	<−5.39	18
2MASSI J1721039+334415	2M1721+33	L3	9	16.31 ± 0.06	12	−1855.601 ± 0.358	591.642 ± 0.369	12	<−5.51	18
2MASS J17502484-0016151	2M1750-00	L4.5	3	9.24 ± 0.02	12	−397.154 ± 0.456	197.921 ± 0.402	12	−6.2 ± 0.1	20
2MASS J18212815+1414010	2M1821+14	L4.5	2	9.36 ± 0.02	12	227.324 ± 0.54	−246.409 ± 0.553	12	⋯	⋯
2MASS J21481628+4003593	2M2148+40	L6	2	8.11 ± 0.03	12	773.298 ± 0.701	458.01 ± 0.884	12	⋯	⋯

Note. Blanks indicate no measurement.

References. (1) Kirkpatrick et al. (2000), (2) Metchev et al. (2015), (3) Schneider et al. (2014), (4) Salim et al. (2003) (5) Cruz et al. (2003), (6) Chiu et al. (2006), (7) Kendall et al. (2007), (8) Reid et al. (2008), (9) Schmidt et al. (2007), (10) Faherty et al. (2012), (11) Smart et al. (2013), (12) Gaia Collaboration et al. (2018), (13) Faherty et al. (2009), (14) Jameson et al. (2008), (15) Schmidt et al. (2010), (16) Faherty et al. (2016), (17) Liu et al. (2016), (18) Schmidt et al. (2015), (19) Reiners & Basri (2008), (20) Pineda et al. (2016), (21) Schmidt et al. (2010).

Table 2
Variability Information of the L Dwarfs in Our Sample

Name	Filter	Amp.	% P2P	Periodic	References	Note
2MASSI J0030300-145033	Ks	0.19 ± 0.11	1.32	yes	EBB03	Ks = 14.38 ± 0.08
	JHKs	0	0	⋯	KO05	
	JHKs	0	0	⋯	CL08	
	izJ	0	0	⋯	SC15	
	J	0	0	⋯	RA14b	
2MASSI J0103320+193536	3.6 μm	0.56 ± 0.03%	0.56 ± 0.03	yes	ME15	
	4.5 μm	0.87 ± 0.09%	0.87 ± 0.09	yes	ME15	
	Ks	0.10 ± 0.02	0.71	yes	EBB03	Ks = 14.15 ± 0.07
	Js	0	0	⋯	VO18	
2MASS J01075242+0041563	3.6 μm	1.27 ± 0.13%	1.27 ± 0.13	no	ME15	
	4.5 μm	1.0 ± 0.2%	1.0 ± 0.2	no	ME15	
2MASSW J0310599+164816	*J*	2%/hr	1.5	unknown	BU14	Assuming $P_{\rm rot}$ = 2× observation length
2MASS J08354256-0819237	*I*	0.01	0.06	yes	KO04a	*I* = 17.6
	Js	1.3 ± 0.2%	1.3 ± 0.2	yes	RA14b	
	Rc	0	0	⋯	KO05	
	Js	1.6 ± 0.5%	1.6 ± 0.5	yes	WI14	
	0.9 μm	0	0	⋯	SC17	
	0.96 μm	0	0	⋯	SC17	
	1.02 μm	0	0	⋯	SC17	
	1.08 μm	0	0	⋯	SC17	
	1.14 μm	0	0	⋯	SC17	
	1.20 μm	0	0	⋯	SC17	
	1.26 μm	0	0	⋯	SC17	
	1.33 μm	0	0	⋯	SC17	
	1.39 μm	0	0	⋯	SC17	
	1.45 μm	0	0	⋯	SC17	
	1.51 μm	0	0	⋯	SC17	
	1.57 μm	0	0	⋯	SC17	
	1.63 μm	0	0	⋯	SC17	
	1.69 μm	0	0	⋯	SC17	
	1.76 μm	0	0	⋯	SC17	
	1.82 μm	0	0	⋯	SC17	
	1.88 μm	0	0	⋯	SC17	
	1.94 μm	0	0	⋯	SC17	
	2.00 μm	0	0	⋯	SC17	
	2.06 μm	0	0	⋯	SC17	
	2.12 μm	0	0	⋯	SC17	
	2.19 μm	0	0	⋯	SC17	
	2.25 μm	0	0	⋯	SC17	
	2.31 μm	0	0	⋯	SC17	
	2.37 μm	0	0	⋯	SC17	
2MASS J10101480-0406499	Js	3.6 ± 0.4%	3.6 ± 0.4	yes	RA14b	
	Js	5.1 ± 1.1%	5.1 ± 1.1	yes	WI14	
2MASS J10433508+1213149	3.6 μm	1.54 ± 0.15%	1.54 ± 0.15	no	ME15	
	4.5 μm	1.2 ± 0.2%	1.2 ± 0.2	no	ME15	
2MASS J10584787-1548172	3.6 μm	0.39 ± 0.04%	0.39 ± 0.04	yes	ME15	
	4.5 μm	0	0	⋯	ME15	
	I	0	0	⋯	KO13	
	R	0	0	⋯	KO13	
	3.6 μm	0.388 ± 0.043%	0.388 ± 0.043	yes	HE13	
	4.5 μm	0.090 ± 0.056%	0.090 ± 0.056	yes	HE13	
	J	0.843 ± 0.098%	0.843 ± 0.098	yes	HE13	
2MASS J12195156+3128497	*J*	∼3–6%/hr	∼2.5–5	unknown	BU14	
	H	0	0	⋯	BU14	
2MASS J14252798-3650229	*J*	0.6 ± 0.1%	0.6 ± 0.1	yes	RA14b	
	Js	0.7 ± 0.3%	0.7 ± 0.3	yes	VO18	
2MASS J16154255+4953211	3.6 μm	0.9 ± 0.2%	0.9 ± 0.2	yes	ME15	
	4.5 μm	0	0	⋯	ME15	
	J	0	0	⋯	VO18	
2MASS J16322911+1904407	*J*	0	0	⋯	BU14	
	H	0	0	⋯	BU14	
	Js	0	0	⋯	WI14	
	3.6 μm	0.42 ± 0.08%	0.42 ± 0.08	yes	ME15	
	4.5 μm	0.5 ± 0.3%	0.5 ± 0.3	yes	ME15	

Table 2
(Continued)

Name	Filter	Amp.	% P2P	Periodic	References	Note
2MASS J17114573+2232044	J	0.206 ± 0.041	1.21	yes	KH13	$J = 17.09 \pm 0.18$
	K'	1.186 ± 0.083	8.05	yes	KH13	$K = 14.73 \pm 0.10$; Comparison stars not stable
	J	0	0	⋯	BU14	
2MASSI J1721039+334415	3.6 μm	0.33 ± 0.07%	0.33 ± 0.07	yes	ME15	
	4.5 μm	0	0	⋯	ME15	
2MASS J17502484-0016151	I	0	0	⋯	KO13	
	R	0	0	⋯	KO13	
	J	0.75%/hr	0.5	unknown	BU14	Assuming $P_{\rm rot} = 2\times$ observation length
	H	0	0	⋯	BU14	
	J	0	0	⋯	RA14b	
2MASS J18212815+1414010	I	0	0	⋯	KO13	
	R	0	0	⋯	KO13	
	3.6 μm	0.54 ± 0.05%	0.54 ± 0.05	yes	ME15	
	4.5 μm	0.71 ± 0.14%	0.71 ± 0.14	yes	ME15	
	1.1–1.7 μm	1.77 ± 0.11%	1.77 ± 0.11	unknown	YA15	
	1.4 μm	1.54 ± 0.21%	1.54 ± 0.21	unknown	YA15	
	0.9 μm	0	3	yes	SC17	
	0.96 μm	0	2.5	yes	SC17	
	1.02 μm	0	2.5	yes	SC17	
	1.08 μm	0	1.8	yes	SC17	
	1.14 μm	0	1.8	yes	SC17	
	1.20 μm	0	1.5	yes	SC17	
	1.26 μm	0	1.3	yes	SC17	
	1.33 μm	0	1.3	yes	SC17	
	1.39 μm	0	1.3	yes	SC17	
	1.45 μm	0	1.3	yes	SC17	
	1.51 μm	0	0.9	yes	SC17	
	1.57 μm	0	0.8	yes	SC17	
	1.63 μm	0	0.7	yes	SC17	
	1.69 μm	0	0.5	yes	SC17	
	1.76 μm	0	0	⋯	SC17	
	1.82 μm	0	0	⋯	SC17	
	1.88 μm	0	0	⋯	SC17	
	1.94 μm	0	0.6	yes	SC17	
	2.00 μm	0	0	⋯	SC17	
	2.06 μm	0	0	⋯	SC17	
	2.12 μm	0	0	⋯	SC17	
	2.19 μm	0	0	⋯	SC17	
	2.25 μm	0	0	⋯	SC17	
	2.31 μm	0	0	⋯	SC17	
	2.37 μm	0	0	⋯	SC17	
2MASS J21481628+4003593	J	0	0	⋯	KH13	
	3.6 μm	1.33 ± 0.07%	1.33 ± 0.07	yes	ME15	
	4.5 μm	1.03 ± 0.1%	1.03 ± 0.1	yes	ME15	

Note. Amplitude units are in magnitudes unless otherwise noted.
References. (BU14) Buenzli et al. (2014), (CL08) Clarke et al. (2008), (EBB03) Enoch et al. (2003), (HE13) Heinze et al. (2013), (KH13) Khandrika et al. (2013), (KO04a) Koen (2004), (KO13) Koen (2013), (KO05) Koen (2005), (ME15) Metchev et al. (2015), (RA14b) Radigan (2014), (SC17) Schlawin et al. (2017), (SC15) Schmidt et al. (2015), (VO18) Vos et al. (2018), (WI14) Wilson et al. (2014), (YA15) Yang et al. (2015).

2MASS J10433508+1213149. 2M1043+12 was discovered by Chiu et al. (2006) using SDSS data and classified as an L9 dwarf by Schneider et al. (2014). Metchev et al. (2015) determined an irregular rotation period of 3.8 ± 0.2 hr with a variation in the Spitzer IRAC channels 1 and 2 of 1.54 ± 0.15% and 1.2 ± 0.2%, respectively. There have been no Hα observations of 2M1043+12.

DENIS-P J1058.7-1548. DENIS 1058-15 was discovered by Tinney et al. (1997) and was classified as an L2.5 dwarf by Schneider et al. (2014). Heinze et al. (2013) reported a rotation period of $4.25^{+0.26}_{-0.16}$ hr with a variability amplitude of 0.39 ± 0.04% at 3.6 μm and 0.090 ± 0.056% at 4.5 μm. The authors also determine an amplitude of 0.843 ± 0.098% in the J band with a rotation period of 4.31 hr. Metchev et al. (2015) independently confirmed the IRAC amplitudes, measuring a rotation period of 4.1 ± 0.2 hr. Observations by Koen (2013) revealed no variability in the IR bands. Schmidt et al. (2015) measured the Hα activity of DENIS 1058-15 to be $\log(L_{\rm H\alpha}/L_{\rm bol}) = -5.59$.

2MASS J12195156+3128497. 2M1219+31 was identified and classified as an L8 dwarf by Chiu et al. (2006). There is currently no measured rotation period. Buenzli et al. (2014)

tentatively reported an ∼3%–6% per hour amplitude variation from 1.12–1.20 μm and no variability from 1.32–1.66 μm. There have been no Hα observations of 2M1219+31.

2MASS J14252798-3650229. 2M1425-36 was discovered by Kendall et al. (2004) and is an L3 dwarf in the optical (Siegler et al. 2007) and an L5 dwarf in the IR (Kendall et al. 2007). Radigan (2014) measured a rotation period of 3.7 ± 0.8 hr based on *J* band variability with an amplitude of 0.6 ± 0.1%. Vos et al. (2019) similarly reported a *J* band variability amplitude of 0.7 ± 0.3. Schmidt et al. (2015) placed an upper limit on the Hα activity of 2M1425-36 of $\log(L_{H\alpha}/L_{bol}) < -5.03$.

2MASS J16154255+4953211. 2M1615+49 was discovered by and classified as an L4β by Reid et al. (2008). Using the Spitzer IRAC channel 1 and channel 2, Metchev et al. (2015) identified photometric amplitudes of 0.9 ± 0.2% and <0.39% in these channels, respectively. The authors also reported a rotation period of ∼24 hr. Vos et al. (2019) observed no variability in the *J* band. There have been no Hα observations of 2M1615+49.

2MASS J16322911+1904407. 2M1632+19 was discovered by Kirkpatrick et al. (1999) and is an L8 dwarf (Schneider et al. 2014). While no variability has been reported in the J and H bands (Buenzli et al. 2014; Wilson et al. 2014), Metchev et al. (2015) observed variability amplitudes of 0.42 ± 0.08% at 3.6 μm and 0.5 ± 0.3% at 4.5 μm. The authors determined a regular rotation period of 3.9 ± 0.2 hr. Two previous surveys have searched for auroral emission but were only able to report upper limits: Route & Wolszczan (2013) observed at 5 GHz with Arecibo and placed a limit of <54 μJy, while Antonova et al. (2008) used the VLA at 4.9 GHz to place a limit of <39 μJy. Schmidt et al. (2015) placed an upper limit on the Hα activity of 2M1632+19 of $\log(L_{H\alpha}/L_{bol}) < -5.52$.

2MASS J17114573+2232044. 2M1711+22 was discovered by Kirkpatrick et al. (2000) and was identified as an L9.5 dwarf by Schneider et al. (2014). Khandrika et al. (2013) reported J and K variability at 0.103 ± 0.041 mag semi-amplitude and 0.593 ± 0.083 mag semi-amplitude, respectively. Buenzli et al. (2014) saw no variability in the *J* band. Schmidt et al. (2015) placed an upper limit on the Hα activity of 2M1711+22 of $\log(L_{H\alpha}/L_{bol}) < -5.39$.

2MASSI J1721039+334415. 2M1721+33 was discovered by Cruz et al. (2003) and is an L3 dwarf (Schmidt et al. 2007) with a rotation period of 2.6 ± 0.1 hr (Metchev et al. 2015). Metchev et al. (2015) observed amplitude variations of 0.33 ± 0.07% at 3.6 μm and <0.29% at 4.5 μm. Berger (2006) searched for radio activity and reported an upper limit of 48 μJy. Schmidt et al. (2015) placed an upper limit on the Hα activity of 2M1721+33 of $\log(L_{H\alpha}/L_{bol}) < -5.51$.

2MASS J17502484-0016151. 2M1750-00 was discovered by Kendall et al. (2007) and classified as an L4.5 dwarf by Schneider et al. (2014). Its rotation period is currently unknown, but Buenzli et al. (2014) observed a photometric amplitude change of ∼0.7% per hour using HST/WFC3 in the J broad band over a 40 minutes observation period. They report no variability in the H broad band. Koen (2013) and Radigan (2014) observed no variability in the I, R, and J bands, respectively. Antonova et al. (2013) searched for radio emission using the VLA but reported a non-detection with 43 μJy sensitivity. Additionally, Pineda et al. (2016) measured the Hα activity of 2M1750-00 to be $\log(L_{H\alpha}/L_{bol}) = -6.2 \pm 0.1$.

2MASS J18212815+1414010. 2M1821+14 was discovered by Looper et al. (2008) and was classified as an L4.5 dwarf (Metchev et al. 2015). Metchev et al. (2015) determined an irregular rotation period of 4.2 ± 0.1 hr, with photometric amplitudes of 0.54 ± 0.05% at 3.6 μm and 0.71 ± 0.14% at 4.5 μm. Yang et al. (2015) observed from 1.1–1.7 μm, seeing a 1.77 ± 0.11% amplitude out of the water band (1.4 μm), and a 1.54 ± 0.21% amplitude at the water band. In a dedicated study, Schlawin et al. (2017) demonstrated that there is a steady decrease in variability amplitude from 0.9–2.4 μm starting at 1.5% semi-amplitude at 0.9 μm, eventually decreasing to 0% at ∼1.7 μm, where it remains through 2.4 μm. Koen (2013) reported no variability in the *IR* bands. There have been no Hα observations of 2M1821+14.

2MASS J21481628+4003593. 2M2148+40 was discovered by Looper et al. (2008) and was classified as an L6 dwarf (Metchev et al. 2015). Metchev et al. (2015) determined a rotation period of 19 ± 4 hr, with photometric amplitudes of 1.33 ± 0.07% at 3.6 μm and 1.03 ± 0.1% at 4.5 μm. Khandrika et al. (2013) reported no variability in the *J* band. Antonova et al. (2013) reported a non-detection at 4.9 GHz using the VLA with a sensitivity of 63 μJy. There have been no Hα observations of 2M2148+40.

3. Observations

We observed the 17 targets with the Karl G. Jansky VLA at *C*-band (4–8 GHz). We used the WIDAR correlator in 3 bit observing mode for 4 GHz bandwidth observations with 2 s integrations in 2 hr time blocks for 34 total program hours. We used the full 4 GHz bandwidth available to achieve ∼3 μJy sensitivity. Observations were made between 2016 April–August at C, CnB (i.e., while the VLA was moving from C to B configuration), and B configurations. Since our targets are point sources and not resolved, the configuration did not affect the results of our survey. The observations are summarized in Table 3.

3.1. Calibrations

We calibrated our measurement sets using `Common Astronomy Software Applications (CASA)` version 5.6.1-8 packages. Raw measurement sets were calibrated with the VLA Calibration Pipeline using the flux and phase calibrators in Table 3, after which we manually flagged the radio frequency interference (RFI). Flux calibrators were observed once during each observing block, and flux bootstrapping results in an absolute flux calibration accuracy of ∼5%. Phase calibrators were within 10 degrees of each target and of S or P quality for *C*-band at our configurations. To calibrate complex gain solutions, we alternated between phase calibrator and target with cycle times of ∼30 minutes.

3.2. Source Motion

We corrected the 2MASS coordinates (Skrutskie et al. 2006) of our targets to determine expected positions using the proper-motion measurements listed in Table 3. We phase-centered each object to these coordinates with `fixvis` before using the `clean` routine to image each target.

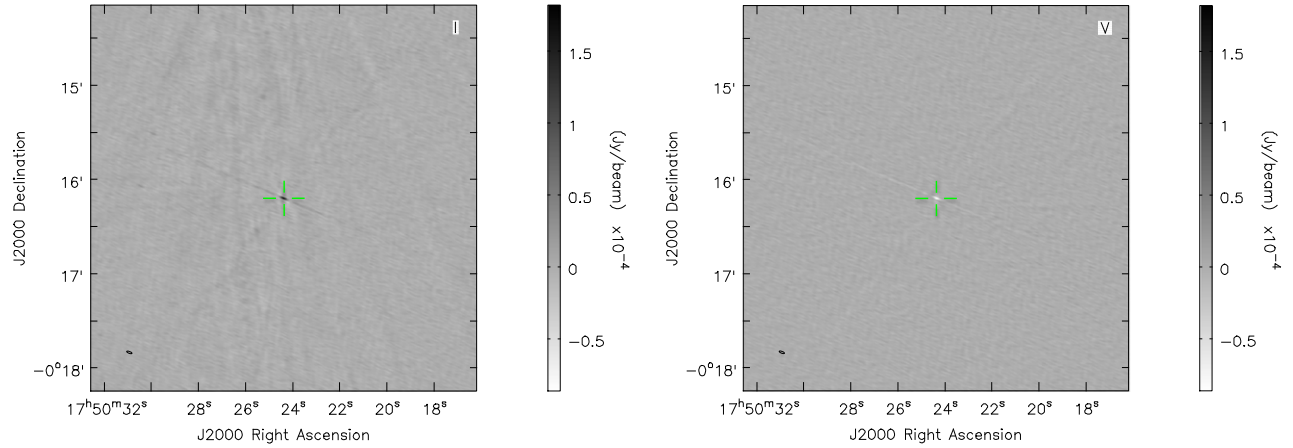

Figure 1. Stokes *I* (left) and Stokes *V* (right) images of 2M1750-00. The cross-hairs denote the calculated proper-motion-corrected coordinates of our target. The synthesized beam is seen in the lower-left corner.

Table 3
Observation Summary of Our Sample

Object	Band (GHz)	Obs. Date (2016)	Obs. Block (hr)	Time on (s)	VLA Config.	Synthesized Beam Size ($'' \times ''$)	f_ν[a] Stokes *I* (μJy)	f_ν[a] Stokes *V* (μJy)	$\log_{10}(L_\nu)$ Stokes *I*, *V* (erg s^{-1} Hz^{-1})	Phase Calibrator	Flux Calibrator
2M0030-14	4–8	1-May	2	5470	CnB	2.78 × 1.54	<17.4	<11.4	<13.2, <13.0	J0050-0929	3C48
2M0103+19	4–8	8-Apr	2	5644	C	2.98 × 2.77	<11.4	<9.9	<12.8, <12.7	J0112+2244	3C48
2M0107+00	4–8	2-Jun	2	5290	B	1.01 × 0.92	<10.2	<9.0	<12.5, <12.4	J0059+0006	3C48
2M0310+16	4–8	6-May	2	5546	CnB	3.41 × 0.99	<10.8	<10.2	<13.0, <13.0	J0318+1628	3C48
2M0835-08	4–8	6-Jun	2	5112	B	1.59 × 0.93	<14.7	<13.8	<12.0, <11.9	J0820-1258	3C286
2M1010-04	4–8	10-May	2	5408	CnB	3.21 × 1.29	<47.4	<14.4	<13.2, <12.7	J1024-0052	3C286
2M1043+12	4–8	14-Jun	2	4992	B	0.95 × 0.88	<12.6	<12.0	<12.5, <12.5	J1120+1420	3C286
DENIS 1058-15	4–8	10-May	2	5466	CnB	3.47 × 1.45	<10.5	<9.9	<12.6, <12.6	J1039-1541	3C286
2M1219+31	4–8	11-Jun	2	5290	B	1.18 × 0.88	<14.1	<13.2	<12.7, <12.7	J1221+2813	3C286
2M1425-36	4–8	5-May	2	5524	CnB	3.13 × 2.46	<12.9	<12.0	<12.3, <12.3	J1356-3421	3C147
2M1615+49	4–8	4-May	2	5670	CnB	2.98 × 1.01	<9.0	<9.6	<13.0, <13.0	J1620+4901	3C147
2M1632+19	4–8	15-May	2	5406	CnB	3.71 × 1.06	<10.8	<11.1	<12.5, <12.5	J1640+1220	3C286
2M1711+22	4–8	17-May	2	5406	CnB → B	1.52 × 0.86	<11.4	<9.6	<13.1, <13.0	J1716+2152	3C286
2M1721+33	4–8	4-May	2	5520	CnB	5.62 × 1.03	<11.4	<11.1	<12.6, <12.5	J1721+3542	3C286
2M1750-00	4–8	5-May	2	5424	CnB	3.5 × 1.19	185 ± 18	−88 ± 11	13.3, 13.0	J1804+0101	3C286
2M1821+14	4–8	14-Aug	2	5262	B	1.67 × 0.86	<12.9	<12.3	<12.1, <12.1	J1824+1044	3C286
2M2148+40	4–8	30-May	2	5230	B	0.92 × 0.77	<9.6	<10.2	<11.9, <11.9	J2202+4216	3C48

Note.
[a] Upper limits are $3\sigma_{\rm rms}$ where $\sigma_{\rm rms}$ is the rms noise in each image. For measured flux densities, positive and negative values correspond to right and left circular polarization, respectively.

4. Results

4.1. Imaging

We produced Stokes *I* and Stokes *V* (total and circular polarization, respectively) images using the `CASA` task `clean`. We used a Brigg's weighting of 0.0, which gives a good trade-off between sensitivity and resolution. We searched for a point source at the proper-motion-corrected coordinates in each image. We self-calibrated one target, 2M1010+00, to mitigate phase errors in three brighter (∼3–11 mJy) objects in the field and improved the rms noise in the image by 25%. We detect radio emission in Stokes *I* and Stokes *V* from one target in our sample, 2M1750-00, seen in Figure 1.

We used the `CASA` task `imfit` to determine the position for 2M1750-00 and measure the mean flux density by fitting an elliptical Gaussian point source to the cleaned image. The mean flux density was $185 \pm 18\,\mu$Jy (S/N ∼ 40) in Stokes *I* and $-88 \pm 11\,\mu$Jy (S/N ∼ 25) in Stokes *V* and is unresolved, with a source size of $3\farcs61 \times 1\farcs14$. 3σ upper limits for undetected sources are listed in Table 3.

4.2. Time Series

In addition to visual inspection, we performed a time-series analysis of each target. Following the procedure outlined in Kao et al. (2018), we used the `CASA` task `plotms` to export the real uv visibilities in the rr and ll correlations, averaged across all baselines, channels, and spectral windows. We created time series of both the rr and ll correlations and calculated the Stokes *I* and *V* flux densities as a function of time averaged over the entire 4–8 GHz bandwidth.

We additionally averaged the measurement sets with time resolutions of 10 s, 30 s, and 60 s and frequency resolutions of 2 GHz to search for emission that may have been averaged out in the time-averaged images. We do not detect any statistically significant radio emission in the time series of any additional objects. For 2M1750-00, time series at all time resolutions show

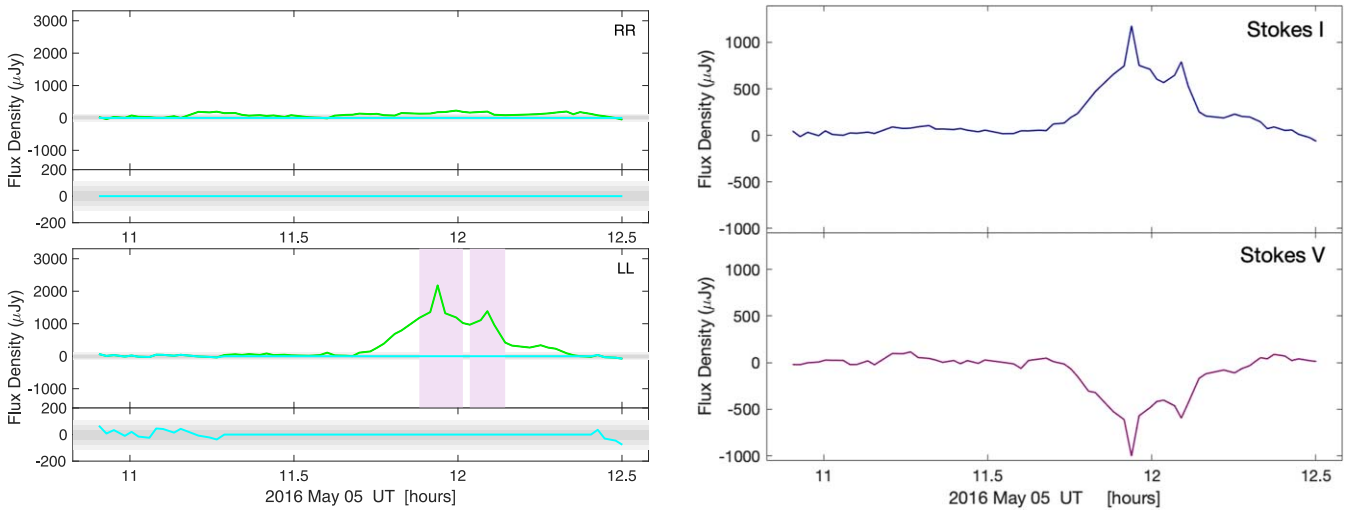

Figure 2. (Left) The right- and left-handed correlations of 2M1750-00 from 4–8 GHz with 2 second integrations. The green lines represent the smoothed data while the cyan line shows the level of quiescent emission after removing the circularly polarized flare. Gray regions are the 1σ, 2σ, and 3σ detection limits. We see one pulse over the course of the two-hour observation, implying a rotation period $\geqslant$2 hr. There is a clear broad peak in emission that has definite substructure (highlighted). (Right) Same as left image but presented in Stokes *I* and Stokes *V*, total intensity and circularly polarized emission, respectively.

a single, highly circularly polarized flare with a double-peaked morphology (Figure 2), implying a rotation period $\geqslant$2 hr.

For each peak in the observed flare from 2M1750-00, we image over the full-width half-maximum (FWHM) of the peak and measure the average Stokes *I* and Stokes *V* flux densities of the flaring emission using the `CASA` task `imfit`. We additionally measure the non-flaring quiescent emission by subtracting the full width of the peak, defined as three times the FWHM of each peak of the flare, from the data.

We report the polarization characteristics of the flaring and non-flaring emission in Table 4. The flux densities of the peaks of the flare are between 8–17 times stronger than quiescent emission in Stokes *I* and 11–22 times stronger in Stokes *V*. The fractional circular polarization for the flaring emission is $72.0\%^{+10.3}_{-14.3}$ for the first peak and $72.8\%^{+17.7}_{-20.4}$ for the second peak, consistent with measurements of highly circularly polarized ECM emission seen by Hallinan et al. (2007) and theoretically predicted by Treumann (2006).

4.3. Dynamic Spectrum of 2M1750-00

We explore the frequency and temporal dependencies of the flare from 2M1750-00 by creating a dynamic spectrum (Figure 3). Using the `CASA` task `plotms`, we exported the real uv visibilities in the rr and ll correlations, averaged across all baselines and channels. We then calculated the Stokes *I* and *V* flux densities for each time and frequency element. Four main vertical gaps in time are marked in white where the phase calibrator observations took place, along with three horizontal gaps in frequency where a significant amount of data was flagged and removed due to RFI. We find that there is clear substructure within the one flare and that emission continues throughout the entire 4–8 GHz bandwidth. Similar cases of substructure have been observed in the radio aurorae for LSR J1835+3259 (Hallinan et al. 2015) and 2M1047 +21 (Williams & Berger 2015; Kao et al. 2018). The underlying mechanism of this substructure remains unknown; however, Hallinan et al. (2015) speculate that this substructure is likely due to contributions from individual, small-scale current systems, similar to what was surmised for the fine structure in the auroral kilometric radiation observed from Jupiter and Saturn (Gurnett et al. 1981; Pottelette et al. 1999; Treumann 2006, and references therein). Given the prevalence of such substructure, understanding the physical driving mechanism of this emission is imperative.

Table 4
Time- and Frequency-integrated Flux Density Measurements of 2M1750-00

Temporal Segment	f_ν, Stokes *I* (μJy)	f_ν, Stokes *V* (μJy)	Circ. Pol. [%]
All	185 ± 18	-88 ± 11	$-47.1^{+18.9}_{-30.0}$
Peak 1	926 ± 40	-667 ± 26	$-72.0^{+10.3}_{-14.3}$
Peak 2	487 ± 20	-355 ± 27	$-72.8^{+17.7}_{-20.4}$
Quiescent	56.4 ± 5.5	31.9 ± 6.6	$56.0^{+41.5}_{-35.0}$

4.4. Lower Limits on the Large-scale Magnetic Field Strength of 2M1750-00

The disk-averaged brightness temperature of the detected flare from 2M1750-00 is $\geqslant 10^{12.6}$ K. Full rotational phase coverage is needed to confirm if the observed flare is periodic on rotational timescales. Nevertheless, the short duration of the flare compared to its $\gtrsim$160 minutes rotation period, inferred from infrared photometric monitoring (Buenzli et al. 2014), is consistent with a flare source region that is much smaller than the disk size of the dwarf. This high minimum brightness temperature together with the strong circular polarization observed during the pulse is consistent with a coherent emission process, as is the case for plasma or ECMI emission.

Plasma emission is emitted at the local plasma frequency $\nu_{\rm pe} = [e^2 n_e/(\pi m_e)]^{1/2} \approx 9 n_e^{1/2}$ kHz or its second harmonic $2\nu_{\rm pe}$. The 4–8 GHz flare detected from 2M175-00 would imply coronal plasma densities on the order of $n_e \sim 10^{11}$ for plasma emission, which exceed expected densities for active M dwarfs (Villadsen & Hallinan 2019). Recent detections of white-light flares on an L2.5 dwarf (Jackman et al. 2019) demonstrate that strong flares persist in early L dwarfs. However, such flares occur less frequently in early L dwarfs compared to M dwarfs (e.g., Schmidt et al. 2016; Paudel et al. 2018, 2020). Furthermore, X-ray emission that correlates with hot coronal plasma is underluminous for L dwarfs compared to their radio emission (Williams et al. 2014). This suggests that the plasma densities in L dwarf atmospheres are less than those of active M dwarfs, which can emit electron cyclotron

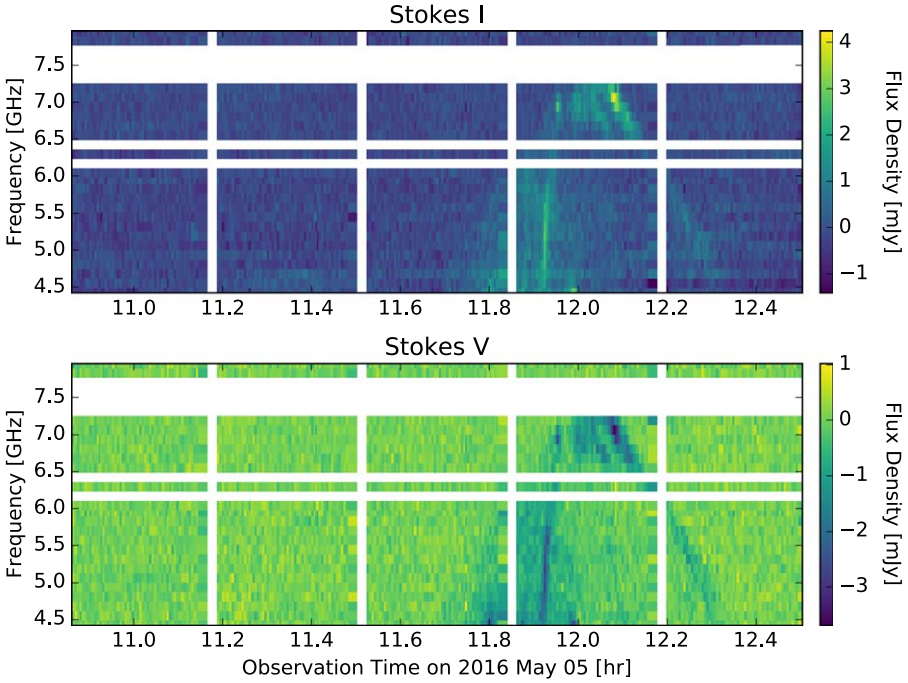

Figure 3. Dynamic spectrum of 2M1750-00 with flux density relative to the average. White regions represent the times where phase calibrator observations took place or frequencies at which significant data was removed due to RFI. We find that the ECM flare from this object is characterized by a broad peak in emission that has substructure. The emission occurs throughout the entire 4–8 GHz bandwidth, implying a magnetic field strength $\geqslant$2.9 kG.

maser emission (Osten & Bastian 2006; Villadsen & Hallinan 2019). We conclude that the flare observed on 2M1750-00 is likely attributable to ECMI emission.

For low plasma densities where the ratio of plasma frequency to cyclotron frequency $<$0.3, ECM instability emission is expected to be produced at the fundamental cyclotron frequency $\nu_{[\mathrm{MHz}]}$ (Melrose et al. 1984; Treumann 2006):

$$\nu_{[\mathrm{MHz}]} \sim 2.8 \times B_{[\mathrm{Gauss}]}. \quad (1)$$

The flare on 2M1750-00 persists throughout our frequency band between 4 and 8 GHz. If the observed flare from 2M1750-00 is indeed produced via the ECMI, we can constrain the local magnetic field strength of the brown dwarf to $\geqslant$2.9 kG. Observations of 2M1750-00 above 8 GHz will be required to assess the upper limit of the magnetic field strength of this target.

4.5. Occurrence Rates of Quiescent Radio Activity

While the detection rate of our survey agreed with typical volume-limited surveys at $\sim$6%, we also calculate the underlying occurrence rate of quiescent radio emission. Detectable levels of quiescent radio emission have been observed in all previous observations of periodically pulsed auroral emission, and is therefore considered a proxy for auroral activity. While the source of the quiescent emission is unconfirmed, it has been speculated that it may trace extrasolar analogs to the Jovian radiation belts, where high-energy electrons are trapped by the magnetosphere (Hallinan et al. 2006; Pineda et al. 2017; Kao et al. 2019). The large (kG) magnetic fields of brown dwarfs and surrounding plasma radiation belts may provide the necessary powerhouse and electron reservoir for both the quiescent emission and auroral ECMI emission (Pineda & Hallinan 2018; Kao et al. 2019).

With this aim, we utilized the maximum-likelihood occurrence rate calculation framework developed by M. M. Kao & E. L. Shkolnik (2020, in preparation). This generalized calculation takes into account each object's distance, observational sensitivity, and an assumed intrinsic radio luminosity distribution. For the latter, we assume a uniform distribution over previously observed ultracool dwarf (M7 or later spectral type) quiescent radio luminosities. Detected L and M dwarf luminosities overlap in luminosity range, with $[L_\nu]$ between 12.6–13.6 and 12.4–13.6 erg s^{-1} Hz^{-1}, respectively (M. M. Kao & E. L. Shkolnik 2020, in preparation). In contrast, detected T dwarf luminosities have so far been fainter than detected L dwarf luminosities, with $[L_\nu] \in$ [11.7,12.7] erg s^{-1} Hz^{-1}. Assuming a uniform distribution over the full $[L_\nu] \in$ [11.7,13.6] erg s^{-1} Hz^{-1} luminosity range for detected ultracool dwarf radio emission accounts for the possibility of fainter and heretofore undetected L dwarf emission.

Following M. M. Kao & E. L. Shkolnik (2020, in preparation), we assume a minimum signal-to-noise ratio of 4 for confirmed radio detections and compute the probability density distributions of quiescent radio emission occurrence rates between [0, 1] for each given sample of brown dwarfs. Simulations of sample sizes with 10 and 20 objects show that on average the quiescent radio occurrence rate formalism recovers the simulated emission rate of quiescent radio emission in the population, better than does a detection rate. This is especially the case for samples with rms sensitivities that are on average lower than the literature distribution, which is the case when we include our presented observations.

The two main samples that we compare are L dwarfs with low- and high-amplitude variability. Dissimilar distributions would suggest that high-amplitude variability may be a viable tracer of quiescent radio emission. In the absence of existing empirical measurements of the relative increase in photometric variability amplitudes that may be caused by energy deposition from magnetic field-aligned currents, we test variability amplitude cutoffs between 1% and 3%.

Table 5 shows our input sample of 77 L dwarfs that have been observed at radio frequencies and adhere to the data inclusion policy outlined in M. M. Kao & E. L. Shkolnik

Table 5
Variability Information of L Dwarfs That Have Been Targeted by Radio Searches to Search for Quiescent Emission

Name	SpT	References	f_I[a]	References	Var.	Filter	Amp.	% P2P	Periodic	References	Note
2MASS J00043484-4044058	L5+L5	RE08	100	LY16	⋯	⋯	⋯	⋯	⋯	⋯	No info
2MASS J00303013-1450333	L7V	KI00	<17.4	This work	yes	Ks	0.2	1.39	yes	EBB03	
					yes	Ks	0.19 ± 0.11	1.32	yes	EBB03	Ks = 14.38 ± 0.08
					no	JHK	0	0	⋯	KT05	
					no	*J*	0	0	⋯	RA14a	
					no	*J*	0	0	⋯	SC15	
					no	*J*	0	0	⋯	CL08	
2MASS J00325937+1410371	L9	SC14	<1101	RW13	⋯	⋯	⋯	⋯	⋯	⋯	No info
2MASS J00361617+1821104	L3.5	RE00	152	BE05	no	IR	0	0	⋯	GU09	
					yes	*I*	0.015	0.09	yes	LA07	
					yes	*I*	0.01	0.05	no	MA07	I/R variability anti-correlated
					yes	*R*	0.03	0.19	no	MA07	I/R variability anti-correlated
					yes	*I*	0.016	0.1	no	KO13	long-term var. possible, >56 mmag amp.
					no	*R*	0.007	0.04	no	KO13	
					no	*I*	0	0	⋯	GE02	
					yes	*R*	3.40 ± 0.11%	3.4	yes	CR16	
					yes	*I*	2.11 ± 0.09%	2.11	yes	CR16	
					yes	*z*	2.74 ± 0.08%	2.74	yes	CR16	
					yes	*J*	1.22 ± 0.04%	1.22	yes	CR16	
					yes	*H*	0.45 ± 0.05%	0.45	yes	CR16	
					yes	Ks	1.07 ± 0.08%	1.07	yes	CR16	
					yes	all—RIzJHKs	1.36 ± 0.03%	1.36	yes	CR16	
					yes	3.6 μm	0.47 ± 0.05%	0.47	no	ME15	
					yes	4.5 μm	0.19 ± 0.04%	0.19	no	ME15	
					yes	*I*	1.98–2.20%	2.2	yes	HA13	
2MASSI J0103320+193536	L6V	KI00	<11.4	This work	yes	3.6 μm	0.56 ± 0.03%	0.56	yes	ME15	
					yes	4.5 μm	0.87 ± 0.09%	0.87	yes	ME15	
					yes	Ks	0.10 ± 0.02	0.71	no	EBB03	Ks = 14.15 ± 0.07
					no	Js	0	0	⋯	VO18	
2MASS J01075242+0041563	L8	SC14	<10.2	This work	yes	3.6 μm	1.27 ± 0.13%	1.27	no	ME15	
					yes	4.5 μm	1.0 ± 0.2%	1	no	ME15	
2MASS J01443536-0716142	L6.5	SC14	<33	BE06	yes	*I*	0.06%	0.06	no	KO13	
2MASS J02050344+1251422	L5V	KI00	<48	BE06	⋯	⋯	⋯	⋯	⋯	⋯	No info
2MASS J02052940-1159296	L7+L7	RE06	<30	BE06	⋯	⋯	⋯	⋯	⋯	⋯	No info
2MASS J02511490-0352459	L3	SC07	<36	BE06	no	*I*	0	0	⋯	KO13	
					no	*R*	0	0	⋯	KO13	
	L9	SC14	<30.9	LY16	no	*J*	0	0	⋯	KT05	

Table 5
(Continued)

Name	SpT	References	f_I[a]	References	Var.	Filter	Amp.	% P2P	Periodic	References	Note
2MASS J02550357-4700509											
					no	*H*	0	0	⋯	KT05	
					no	Ks	0	0	⋯	KT05	
2MASS J02572581-3105523	L8.5	SC14	<63.0	LY16	no	Ic	0	0	⋯	KO13	
					no	Js	0	0	⋯	WI14	
					no	*J*	0	0	⋯	RA14a	
2MASSW J0310599+164816	L8V	KI00	<10.8	This work	yes	*J*	2%/hr	1.5	unknown	BU14	Assuming $P_{\rm rot} = 2\times$ observation length
2MASS J03261367+2950152	L4.6V	BG14	<1293	RW13	⋯	⋯	⋯	⋯	⋯	⋯	No info
2MASS J03284265+2302051	L9.5	SC14	<1044	RW13	yes	Ks	0.43 ± 0.16	2.89	no	EBB03	$K = 14.87$
					no	*J*	0	0	⋯	RA14a	
					no	3.6 μm	0	0	⋯	ME15	
					no	4.5 μm	0	0	⋯	ME15	
2MASS J03400942-6724051	L7	FA09	<27.0	LY16	no	Js	⋯	⋯	⋯	WI14	
2MASS J03552337+1133437	L3-L6	GA15b	<45	AN13	no	*I*	⋯	⋯	⋯	KO13	
2MASS J04234858-0414035	L6.5+T2	DU12	54.1	KAO16	yes	Ks	0.30 ± 0.18	2.32	no	EBB03	
					no	*J*	0.015	0	⋯	KT05	
					no	*H*	0.011	0	⋯	KT05	
					no	K	0.002	0	⋯	KT05	
					yes	*J*	0.008 ± 0.0008	0.06	yes	CL08	
					no	*I*	0	0	⋯	KO13	
					no	Js	0	0	⋯	WI14	
2MASS J04390101-2353083	L4.5	SC14	<42	BE06	yes	Js	2.6 ± 0.5%	2.6	yes	WI14	$J = 4.408 \pm 0.029$
					no	Ic	0	0	⋯	KO13	
					no	Ic	0	0	⋯	KO05	
					no	Js	0	0	⋯	RA14b	
2MASS J04455387-3048204	L2	SC07	<66	BE06	no	Ic	0	0	⋯	WI14	
					no	Ic	0	0	⋯	KO13	
					no	Js	0	0	⋯	KO04b	
2MASS J05002100+0330501	L4pec	GA15b	<51	AN13	⋯	⋯	⋯	⋯	⋯	⋯	No info
2MASS J05233822-1403022	L2.5	CR03	<39	BE06	no	Ic	0	0	⋯	WI14	
					no	Ic	0	0	⋯	KO13	
					no	Js	0	0	⋯	KT05	
2MASS J05395200-0059019	L5	SC14	<48	AN13	no	Ic	0	0	⋯	KO13	
					yes	*I*	0.009%	0.009	no	BM01	
					no	*J*	0	0	⋯	BU14	

Table 5
(Continued)

Name	SpT	References	f_l[a]	References	Var.	Filter	Amp.	% P2P	Periodic	References	Note
					no	*H*	0	0	⋯	BU14	
WISEP J060738.65 +242953.4	L9	CA13	15.6	GI16	no	832 nm	0	0	⋯	GI16	
					no	3.6 μm	0	0	⋯	GI16	
					no	4.5 μm	0	0	⋯	GI16	
2MASS J06523073 +4710348	L4.5	BUR10	<33	BE06 —	⋯	⋯	⋯	⋯	⋯	No info	
2MASS J07003664 +3157266	L3+L6.5	DU12	<42	AN13	⋯	⋯	⋯	⋯	⋯	⋯	No info
2MASS J07464256 +2000321	L0+L1.5	DU17	<48	BE06	yes	Cousins I	0.07%	0.07	yes	GE02	$I = 15.11$
					yes	I band	0.46%	0.46	yes	CL02	
					no	R band	0	0	⋯	MA07	
					no	I band	0	0	⋯	MA07	
					yes	*J*	0.05%	0.05	unknown	BL08	$J = 11.74$
					yes	*H*	0.05%	0.05	unknown	BL08	$H = 11.00$
					yes	Ks	0.06%	0.06	unknown	BL08	Ks = 10.49
					yes	Cousins I	0.54%	0.54	yes	KO13	$I = 15.11$
					no	Cousins R	0	0	⋯	KO13	
					yes	I band	1.52%	1.52	yes	HA13	
2MASS J08251968 +2115521	L7.5V	KI00	<45	BE06	yes	*J*	1%/hr	1.51	unknown	BU14	$J = 15.10$; $H = 13.79$
					yes	*H*	1%/hr	1.51	unknown	BU14	Assuming $P_{rot} = 2\times$ observation length
					yes	0.996 μm	11%	11	unknown	GO08	
					yes	1.008 μm	5%	5	unknown	GO08	
					yes	1.065 μm	14%	14	unknown	GO08	
					yes	3.6 μm	0.81 ± 0.08%	0.81	no	ME15	
					yes	4.5 μm	1.4 ± 0.3%	1.4	no	ME15	
2MASS J08283419-1309198	L2	SC02	<63	AN13	⋯	⋯	⋯	⋯	⋯	⋯	No info
2MASS J08300825 +4828482	L9.5	SC14	<87	AN13	⋯	⋯	⋯	⋯	⋯	⋯	No info
2MASS J08354256-0819237	L6.5	SC14	<14.7	This work	yes	*I*	0.016	0.09	yes	KO04a	$I = 17.6$
					yes	Js	1.3 ± 0.2%	1.3	yes	RA14b	
					no	Rc	0	0	⋯	KO05	
					yes	Js	1.6 ± 0.5%	1.6	yes	WI14	
					no	0.9 μm	0	0	⋯	SC17	
					no	0.96 μm	0	0	⋯	SC17	
					no	1.02 μm	0	0	⋯	SC17	
					no	1.08 μm	0	0	⋯	SC17	
					no	1.15 μm	0	0	⋯	SC17	
					no	1.21 μm	0	0	⋯	SC17	
					no	1.27 μm	0	0	⋯	SC17	
					no	1.33 μm	0	0	⋯	SC17	
					no	1.39 μm	0	0	⋯	SC17	

Table 5
(Continued)

Name	SpT	References	f_l[a]	References	Var.	Filter	Amp.	% P2P	Periodic	References	Note
					no	1.45 μm	0	0	⋯	SC17	
					no	1.51 μm	0	0	⋯	SC17	
					no	1.58 μm	0	0	⋯	SC17	
					no	1.64 μm	0	0	⋯	SC17	
					no	1.70 μm	0	0	⋯	SC17	
					no	1.76 μm	0	0	⋯	SC17	
					no	1.82 μm	0	0	⋯	SC17	
					no	1.88 μm	0	0	⋯	SC17	
					no	1.94 μm	0	0	⋯	SC17	
					no	2.01 μm	0	0	⋯	SC17	
					no	2.07 μm	0	0	⋯	SC17	
					no	2.13 μm	0	0	⋯	SC17	
					no	2.19 μm	0	0	⋯	SC17	
					no	2.25 μm	0	0	⋯	SC17	
					no	2.31 μm	0	0	⋯	SC17	
					no	2.37 μm	0	0	⋯	SC17	
2MASS J08503593 +1057156	L6.5+L8.5	DU12	<1302	RW13	⋯	⋯	⋯	⋯	⋯	⋯	No info
2MASS J08575849 +5708514	L7	SC14	<51	AN13	⋯	⋯	⋯	⋯	⋯	⋯	No info
2MASS J09002367 +2539345	L6.7V	BG14	<1906	RW16	⋯	⋯	⋯	⋯	⋯	⋯	No info
2MASS J09083803 +5032088	L8	SC14	<111	AN13	no	JH	0	0	⋯	BU14	
2MASS J09121469 +1459396	L8.5+L7.5	DU12	<1473	RW13	⋯	⋯	⋯	⋯	⋯	⋯	No info
2MASS J09130320 +1841501	L3	FA09	<102	ML12	no	*I*	0	0	⋯	BM99	
2MASS J09230861 +2340152	L2.3V	BG14	<4785	RW16	⋯	⋯	⋯	⋯	⋯	⋯	No info
2MASS J09293364 +3429527	L8V	KI00	<42	BE06	⋯	⋯	⋯	⋯	⋯	⋯	No info
2MASS J10101480-0406499	L6	CR03	<47.4	This work	yes	*J*	3.6 ± 0.4%	3.6	yes	RA14b	
					yes	*J*	5.1 ± 1.1%	5.1	yes	WI14	
2MASS J10292165 +1626526	L2.5	KI00	<33	ML12	no	*I*	0	0	⋯	MA07	
					no	*R*	0	0	⋯	MA07	
					no	*I*	0	0	⋯	GE02	
2MASS J10430758 +2225236	L8.5	SC14	9.5	KAO18	⋯	⋯	⋯	⋯	⋯	⋯	No info
2MASS J10433508 +1213149	L9	SC14	<12.6	This work	yes	3.6 μm	1.54 ± 0.15%	1.54	no	ME15	
					yes	4.5 μm	1.2 ± 0.2%	1.2	no	ME15	
2MASS J10491891-5319100	L7.5+T0.5	BUR13	<15	OS15	yes	0.91 (0.75–1.10) μm	11 ± 1%	11	yes	GI13	B
					yes	0.91 (0.75–1.10) μm	6 ± 1%	6	no	GI13	B

Table 5
(Continued)

Name	SpT	References	f_I[a]	References	Var.	Filter	Amp.	% P2P	Periodic	References	Note
					yes	0.89 (0.81–1.06) μm	7 ± 0.5%	7-11	no	BI13	B
					no	1.23 (1.10–1.40) μm	0	0	⋯	BI13	B
					yes	1.63 (1.50–1.80) μm	13 ± 2%	13	no	BI13	B
					yes	2.16 (1.99–2.35) μm	10 ± 2%	10	no	BI13	B
					yes	0.91 (0.75–1.10) μm	5 ± 1%	5	yes	BUR14	B
					yes	1.00–1.30 μm	7.5%	7.5	no	BUR14	B
					yes	1.1–1.6 μm	7–11%	11	no	BU15a	A—no, aperiodic; B—yes
					yes	0.8–1.15 μm	9.3%	9.3	no	BU15b	B
					yes	0.8–1.15 μm	4.5%	4.5	no	BU15b	A
2MASS J10584787-1548172	L3V	KI99	<10.5	This work	yes	3.6 μm	0.39 ± 0.04%	0.39	yes	ME15	
					no	4.5 μm	0	0	⋯	ME15	
					no	*I*	0	0	⋯	KO13	
					no	*R*	0	0	⋯	KO13	
					yes	3.6 μm	0.388 ± 0.043%	0.388	yes	HE13	
					yes	4.5 μm	0.090 ± 0.056%	0.09	yes	HE13	
					yes	*J*	0.843 ± 0.098%	0.843	yes	HE13	
2MASS J11040127+1959217	L4	SC14	<1381	RW16 —	⋯	⋯	⋯	⋯	⋯	No info	
2MASS J11122567+3548131	L4.5+L6	DU12	<1473	RW13	⋯	⋯	⋯	⋯	⋯	⋯	No info
2MASS J11463449+2230527	L3+L4	PB08	<1146	RW13	no	*I*	0	0	⋯	BM99	
					yes	*I*	0.015	0.09	yes	BM01	$I = 17.62$
					no	*I*	0	0	⋯	GE02	
					no	*I*	0	0	⋯	CL02	
2MASS J12035812+0015500	L5.0V	BG14	<63	ML12	⋯	⋯	⋯	⋯	⋯	⋯	No info
2MASS J12195156+3128497	L9	SC14	<14.1	This work	yes	*J*	3–6%/hr	5	unknown	BU14	Assuming $P_{rot} = 2\times$ observation length
					no	*H*	0	0	⋯	BU14	
2MASS J12281523-1547342	L5.5+L5.5	DU12	<87	BE02 no	Ic	0	0	⋯	KO13		
					no	Js	0	0	⋯	WI14	
2MASS J12560183-1257276 b	L7	GA15a	<9	GU18 —	⋯	⋯	⋯	⋯	⋯	No info	
2MASS J13054019-2541059	L2+L3.5	KO13	<27.6	KR99 yes	857 nm	1.1%	1.1	yes	CL02		
					yes	*I*	1.2%	1.2	yes	CL03	
					yes	g'	0.04%	0.04	yes	LI06	
					no	5900 A	0	0	⋯	LI06	
					yes	*I*	0.0064	0.04	yes	KO13	
					yes	*R*	0.0067	0.03	yes	KO13	$I = 16.85$, R = 19.500

Table 5
(Continued)

Name	SpT	References	f_I[a]	References	Var.	Filter	Amp.	% P2P	Periodic	References	Note
2MASS J13153094-2649513 AB	L5+T7	KI11	370	BUR13	no	*I*	0	0	⋯	KO13	
					no	*I*	0	0	⋯	KO03	
					no	*J*	0	0	⋯	KH13	
					no	K	0	0	⋯	KH13	
2MASS J13285503+2114486	L4.1V	BG14	<1158	RW13	⋯	⋯	⋯	⋯	⋯	⋯	No info
2MASS J14243909+0917104	L4	LE01	<97	BE02	⋯	⋯	⋯	⋯	⋯	⋯	No info
2MASS J14252798-3650229	L4	GA15b	<12.9	This work	yes	*J*	0.6 ± 0.1%	0.6	yes	RA14a	
					yes	Js	0.7 ± 0.3%	0.7	yes	VO18	
2MASS J14460061+0024519	L4.2V	BG14	<1098	RW13	⋯	⋯	⋯	⋯	⋯	⋯	No info
2MASS J15065441+1321060	L3	SC14	<78	ML12	no	*I*	0	0	⋯	MA07	
					no	*R*	0	0	⋯	MA07	
					no	*I*	0	0	⋯	GE02	
2MASS J15074769-1627386	L5V	KI00	<36.6	LY16 no	Ic	0	0	⋯	KO03		
					no	Ic	0	0	⋯	KO13	
					no	Js	0	0	⋯	WI14	
					yes	1.4 μm	40%	40	unknown	YA15	
					no	Js	0	0	⋯	RA14b	
					yes	3.6 μm	0.53 ± 0.11%	0.53	no	ME15	
					yes	4.5 μm	0.45 ± 0.09%	0.45	no	ME15	
2MASS J15150083+4847416	L6.5	CR03	<27	BE06	no	1.1–1.7 μm	0	0	⋯	BU14	
2MASS J15232263+3014562	L8V	KI00	<45	BE06	⋯	⋯	⋯	⋯	⋯	⋯	No info
2MASS J16154255+4953211	L4gamma	CR18	<9.0	This work	yes	3.6 μm	0.9 ± 0.2%	0.9	unknown	ME15	
					no	4.5 μm	0	0	⋯	ME15	
					no	*J*	0	0	⋯	VO18	
2MASS J16154416+3559005	L3V	KI00	<75	ML12	no	*I*	0	0	⋯	GE02	
2MASS J16322911+1904407	L8	SC14	<10.8	This work	no	*J*	0	0	⋯	BU14	
					no	*H*	0	0	⋯	BU14	
					no	Js	0	0	⋯	WI14	
					yes	3.6 μm	0.42 ± 0.08%	0.42	yes	ME15	
					yes	4.5 μm	0.5 ± 0.3%	0.5	yes	ME15	
2MASS J17072343-0558249	M9+L3	RE08	<48	BE06	⋯	⋯	⋯	⋯	⋯	⋯	No info
2MASS J17114573+2232044	L5.0+T5.5	BUR10	<11.4	This work	yes	*J*	0.206 ± 0.041	1.21	yes	KH13	
					yes	K'	1.186 ± 0.083	8.05	yes	KH13	
					no	*J*	0	0	⋯	BU14	

Table 5
(Continued)

Name	SpT	References	f_I[a]	References	Var.	Filter	Amp.	% P2P	Periodic	References	Note
2MASS J17210390 +3344160	L5.3:V	BG14	<48	BE06	yes	3.6 μm	0.33 ± 0.07%	0.33	yes	ME15	
					no	4.5 μm	0	0	⋯	ME15	
2MASS J17281150 +3948593	L5+L6.5	GE14	<54	BE06	⋯	⋯	⋯	⋯	⋯	⋯	No info
2MASS J17502484-0016151	L5	KO17	185	This work	no	*I*	0	0	⋯	KO13	
					no	*R*	0	0	⋯	KO13	
					yes	*J*	0.75%/hr	0.5	unknown	BU14	Assuming $P_{rot} = 2\times$ observation length
					no	*H*	0	0	⋯	BU14	
					no	*J*	0	0	⋯	RA14a	
2MASS J18212815 +1414010	L5	SC14	<12.9	This work	no	*I*	0	0	⋯	KO13	
					no	*R*	0	0	⋯	KO13	
					yes	3.6 μm	0.54 ± 0.05%	0.54	no	ME15	
					yes	4.5 μm	0.71 ± 0.14%	0.71	no	ME15	
					yes	1.1-1.7 μm	1.77 ± 0.11%	1.77	unknown	YA15	
					yes	1.4 μm	1.54 ± 0.21%	1.54	unknown	YA15	
					yes	0.90	3%	3	yes	SC17	
					yes	0.96	2.5%	2.5	yes	SC17	
					yes	1.02	2.5%	2.5	yes	SC17	
					yes	1.08	1.8%	1.8	yes	SC17	
					yes	1.15	1.8%	1.8	yes	SC17	
					yes	1.21	1.5%	1.5	yes	SC17	
					yes	1.27	1.3%	1.3	yes	SC17	
					yes	1.33	1.3%	1.3	yes	SC17	
					yes	1.39	1.3%	1.3	yes	SC17	
					yes	1.45	1.3%	1.3	yes	SC17	
					yes	1.51	0.9%	0.9	yes	SC17	
					yes	1.58	0.8%	0.8	yes	SC17	
					yes	1.64	0.7%	0.7	yes	SC17	
					yes	1.70	0.5%	0.5	yes	SC17	
					no	1.76	0	0	⋯	SC17	
					no	1.82	0	0	⋯	SC17	
					no	1.88	0	0	⋯	SC17	
					yes	1.94	0.6%	0.6	yes	SC17	
					no	2.01	0	0	⋯	SC17	
					no	2.07	0	0	⋯	SC17	
					no	2.13	0	0	⋯	SC17	
					no	2.19	0	0	⋯	SC17	
					no	2.25	0	0	⋯	SC17	
					no	2.31	0	0	⋯	SC17	
					no	2.37	0	0	⋯	SC17	
2MASS J18410861 +3117279	L4Vpec	KI00	<3696	RW13	⋯	⋯	⋯	⋯	⋯	⋯	No info
2MASS J21011544 +1756586	L7+L8	DU12	<3172	RW13	⋯	⋯	⋯	⋯	⋯	⋯	No info

Table 5
(Continued)

Name	SpT	References	f_I[a]	References	Var.	Filter	Amp.	% P2P	Periodic	References	Note
2MASS J21041491-1037369	L2	SC14	<24	BE06	no	*I*	0	0	⋯	KO13	
					no	JHK	0	0	⋯	KT05	
2MASS J21481633+4003594	L7	SC14	<9.6	This work	no	*J*	0	0	⋯	KH13	
					yes	3.6 μm	1.33 ± 0.07%	1.33	yes	ME15	
					yes	4.5 μm	1.03 ± 0.1%	1.03	yes	ME15	
2MASS J22244381-0158521	L4.5V	KI00	<33	BE06	yes	*I*	0.083	0.46	no	GE02	$I = 18.0$
					no	JHK	0	0	⋯	KO04b	
					no	JHK	0	0	⋯	KT05	
					no	3.6 μm	0	0	⋯	ME15	
					no	4.5 μm	0	0	⋯	ME15	
2MASS J22521073-1730134	L4.5+T3.5	DU12	<30	BE06	no	Js	0	0	⋯	WI14	
					no	*I*	0	0	⋯	KO13	

Notes. We include only spectral types >L2.5 to match those of our target sample. Amplitude units are in magnitudes unless otherwise noted.
[a] Radio fluxes in Stokes I, reported at frequencies between 4 - 12 GHz.

References. (AN13) Antonova et al. (2013), (BE02) Berger (2002), (BE05) Berger et al. (2005), (BE06) Berger (2006), (BG14) Bardalez Gagliuffi et al. (2014), (BI13) Biller et al. (2013), (BL08) Blake et al. (2008), (BM01) Bailer-Jones & Mundt (2001), (BM99) Bailer-Jones & Mundt (1999), (BU14) Buenzli et al. (2014), (BU15a) Buenzli et al. (2015b), (BU15b) Buenzli et al. (2015a), (BUR10) Burgasser et al. (2010), (BUR13) Burgasser et al. (2013), (BUR14) Burgasser et al. (2014), (CA13) Castro et al. (2013), (CL02) Clarke et al. (2002), (CL03) Clarke et al. (2003), (CL08) Clarke et al. (2008), (CR03) Cruz et al. (2003), (CR16) Croll et al. (2016), (CR18) Cruz et al. (2018), (DU12) Dupuy & Liu (2012), (DU17) Dupuy & Liu (2017), (EBB03) Enoch et al. (2003), (FA09) Faherty et al. (2009), (GA15a) Gagné et al. (2015b), (GA15b) Gagné et al. (2015a), (GE02) Gelino et al. (2002), (GE14) Gelino et al. (2014), (GI13) Gillon et al. (2013), (GI16) Gizis et al. (2016), (GO08) Goldman et al. (2008), (GU09) Guenther et al. (2009), (GU18) Guirado et al. (2018), (HA13) Harding et al. (2013), (HE13) Heinze et al. (2013), (KAO16) Kao et al. (2016), (KAO18) Kao et al. (2018), (KH13) Khandrika et al. (2013), (KI00) Kirkpatrick et al. (2000), (KI11) Kirkpatrick et al. (2011), (KI99) Kirkpatrick et al. (1999), (KO03) Koen (2003), (KO04a) Koen (2004), (KO04b) Koen et al. (2004), (KO05) Koen (2005), (KO13) Koen (2013), (KO17) Koen et al. (2017), (KR99) Krishnamurthi et al. (1999), (KT05) Koen et al. (2005), (LA07) Lane et al. (2007), (LE01) Leggett et al. (2001), (LI06) Littlefair et al. (2006), (LY16) Lynch et al. (2016), (MA07) Maiti (2007), (ML12) McLean et al. (2012), (ME15) Metchev et al. (2015), (OS15) Osten et al. (2015), (PB08) Phan-Bao et al. (2008), (RA14a) Radigan et al. (2014), (RA14b) Radigan (2014), (RE00) Reid et al. (2000), (RE06) Reid et al. (2006), (RE08) Reid et al. (2008), (RW13) Route & Wolszczan (2013), (RW16) Route & Wolszczan (2016), (SC02) Scholz & Meusinger (2002), (SC07) Schmidt et al. (2007), (SC14) Schneider et al. (2014), (SC15) Schmidt et al. (2015), (SC17) Schlawin et al. (2017), (VO18) Vos et al. (2018), (WI14) Wilson et al. (2014), (YA15) Yang et al. (2015).

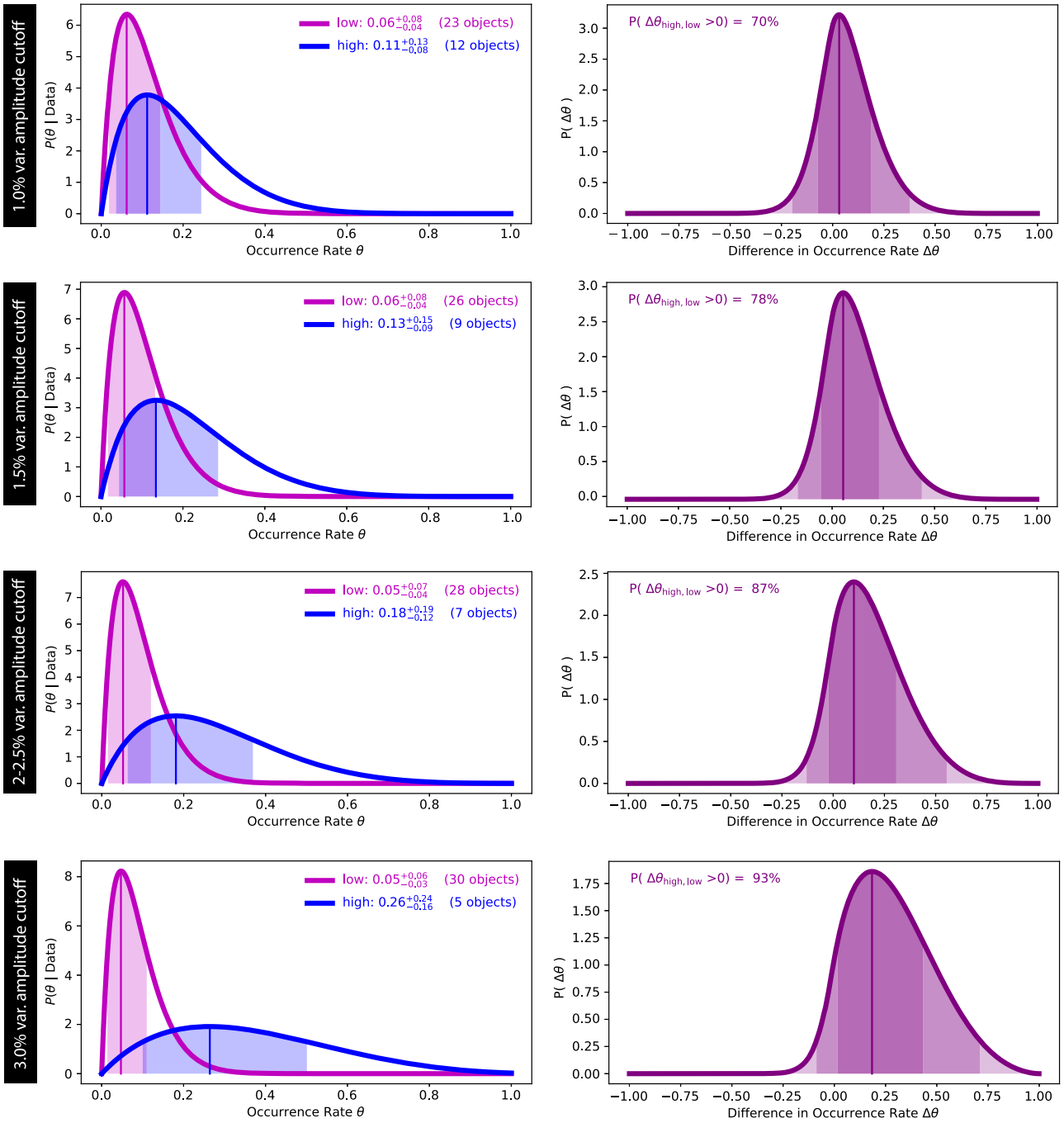

Figure 4. (Left) Quiescent radio occurrence rate distributions for L dwarfs with low vs. high photometric variability amplitudes. Shaded regions show the 68.3% credible intervals. Distributions are calculated using the M. M. Kao & E. L. Shkolnik (2020, in preparation) framework for amplitude cutoffs between [1.0%, 3%]. The 2% and 2.5% cutoff cases are the same, as there were no objects with photometric variability amplitudes between 2% and 2.5%. The maximum-likelihood occurrence rate remains approximately constant for the low-amplitude samples regardless of the amplitude cutoff, while the high-amplitude occurrence rate appears to increase with increasing amplitude cutoff. However, this is an artifact of sample size. (Right) Probability density distributions for the difference in occurrence rates $\Delta\theta$ between high- and low-amplitude samples. Shaded regions correspond to 68.3%, 95.5%, and 99.5% credible intervals. In all cases, we cannot determine if high-amplitude O/IR variability traces radio magnetic activity as our results do not suggest a difference in the radio occurrence rates between high- and low-amplitude variability.

(2020, in preparation). The majority (48) of these objects have been observed for O/IR variability, for which the amplitude, wavelength, and periodicity information is listed. Note that some objects have multiple observations in the same bandpass with both a detection and non-detection of O/IR variability. However, we do not expect the stability of O/IR variability to significantly impact the presence of quiescent radio emission, which observations confirm can persist for at least 10 yr (e.g., Hallinan et al. 2006; Gawroński et al. 2017), since the underlying driving mechanisms are different. In cases where data was re-examined, we defer to the updated results. Finally, we remove all binary objects, as binaries may demonstrate a different occurrence rate distribution than that of single objects (M. M. Kao & E. L. Shkolnik 2020, in preparation). The number of targets in each sample for each cutoff is seen in Table 6.

Figure 4 shows the probability density distributions for the quiescent radio occurrence rate of high-amplitude versus

Table 6
Number of Objects Used in Each Sample with Varying Photometric Amplitude Cutoff

	Number in Sample	
Amp. Cutoff	No/Low-Amp.[a]	High-Amp.[b]
1%	23	12
1.5%	26	9
2%	28	7
2.5%	28	7
3%	30	5

Notes.
[a] No or Low-Amplitude is defined as variability at the percentage below the amplitude cutoff.
[b] High-Amplitude is defined as variability at the percentage above the amplitude cutoff.

low-amplitude objects for different O/IR amplitude cutoffs. We also calculate the probability $P(\Delta\ \theta)$ that the two samples have a difference occurrence rate $\Delta\theta$. The maximum-likelihood occurrence rate increases with increasing photometric variability amplitude cutoff. However, an interpretation of this tentative trend requires an abundance of caution, on which we elaborate in Section 5.1. Furthermore, Figure 4 shows that for all variability amplitudes, our results do not suggest a difference in the radio occurrence rates between high- and low-amplitude variability. In all cases, the occurrence rate for the low-amplitude variable objects remains constant at 5%–6%.

5. Discussion

Kao et al. (2016) demonstrated that Hα and/or O/IR variability trace radio aurorae, and consequently the quiescent radio emission that accompany all instances of radio aurorae, on L and T dwarfs. Miles-Páez et al. (2017) showed that O/IR variability does not trace Hα emission. This is unsurprising, since a significant portion of O/IR variability can be attributed to clouds. Therefore, our work asks whether magnetism, traced by radio emission, enhances O/IR variability.

In this work, we isolated the selection effects of Hα and O/IR variability by focusing on objects with the latter. In contrast to the pilot sample from Kao et al. (2016) in which the authors saw a detection rate of 80%, we see detections in Stokes *I* and Stokes *V* in only one of our 17 targets (6%). Our detection rate is consistent with volume-limited radio surveys that do not bias their target sample with other possible tracers of aurorae (Route & Wolszczan 2012, 2013; Antonova et al. 2013; Lynch et al. 2016).

We must consider the possibility that our observed radio activity detection rate may be a lower limit to the true occurrence rate. For the 16 objects for which no emission was observed, we consider two possibilities that affect observational completeness, including for both quiescent or flaring emission.

First, we may have not observed these targets during a flare. For any target with a rotation period longer than 2 hr, we were not able to observe full coverage of the brown dwarf and thus may have missed when the pulsed emission was beamed toward Earth. However, since quiescent radio emission at 4–8 GHz (Kao et al. 2019) accompanies all known examples of ECM emission from ultracool dwarfs at GHz frequencies. Since we do not detect such emission, these objects likely do not have time-variable ECM emission at our observed frequencies. Long-term monitoring that provides full phase coverage may prove otherwise.

Second, the quiescent emission may be too faint to detect. However, our sensitivities are sufficient to detect quiescent emission for objects emitting at quiescent flux densities that have been observed on L dwarfs, ranging from $[L_\nu] \approx$ 12.6–13.6 erg s^{-1} Hz^{-1} (M. M. Kao & E. L. Shkolnik 2020, in preparation). Therefore, the possibility of quiescent emission that is too faint to be detectable can most likely be ruled out for our sample. Furthermore, the occurrence rate calculation takes observational completeness into account.

We conclude that O/IR variability by itself does not trace aurorae.

5.1. Occurrence Rates of Quiescent Radio Emission

If indeed high-amplitude O/IR variability does not trace quiescent radio emission, we expect the low- and high-amplitude maximum-likelihood occurrence rates to be similar and to not change with varying amplitude cutoff. Conversely, if high-amplitude O/IR variability does trace quiescent radio emission, we expect maximum-likelihood occurrence rates between the two samples to diverge with increasing photometric amplitude cutoff up until the true physical amplitude cutoff that identifies the onset of magnetically driven O/IR variability. Using amplitude cutoffs that are not the true cutoff will result in cross-contaminated samples that reduce the distinction between the two samples.

Even though the maximum-likelihood occurrence rate seems to increase with increasing photometric variability amplitude cutoff (Figure 4), this behavior is a consequence of decreasing sample sizes. The detection rate for a given sample determines the lower bound of the maximum-likelihood occurrence rate. As sample size N decreases, the resolution $1/N$ for detection rates grows. This pushes the maximum-likelihood occurrence rate higher even if the number of detected objects remains the same in each sample. This is the case for our calculations, in which each of the high-amplitude samples that we define with various amplitude cutoffs contain the same single radio-emitting object. Thus, we conclude that the tentative rising radio occurrence rate trend that we observe is most likely an artifact of small sample sizes.

Based on our results, we conclude that observed O/IR variability does not trace radio magnetic activity, as the low radio occurrence rates of both the low- and high-amplitude variability samples are consistent both with each other and with the overall L dwarf population from M. M. Kao & E. L. Shkolnik (2020, in preparation). Comparing this to the prevalence of photometric variability, we infer that optical and infrared variability seen on L dwarfs from 0.5–4.5 μm is likely predominantly due to cloud phenomena.

However, we also consider other possible explanations for the non-distinct occurrence rates that we observe between our low- and high-amplitude samples.

One possibility is geometry. High inclination objects (equator-on) exhibit higher *J* band variability amplitudes, with amplitudes strongly attenuated at lower inclinations (Vos et al. 2017). However, few brown dwarfs have measured inclination angles and existing measurements are not well constrained (Vos et al. 2020). Consequently, our low-amplitude sample may be contaminated by high-amplitude objects at low inclinations. This would cause the radio occurrence rate of the low-amplitude sample to shift toward the high-amplitude

occurrence rate, since we do not anticipate geometric effects to affect the quiescent radio occurrence rate. The occurrence rate framework from M. M. Kao & E. L. Shkolnik (2020, in preparation) considers the non-pulsing quiescent radio component rather than the highly beamed auroral component (M. M. Kao & E. L. Shkolnik 2020, in preparation). Spectral indices measured for brown dwarf quiescent radio emission indicate a gyrosynchrotron mechanism (Williams et al. 2015). While gyrosynchrotron emission from individual electrons is weakly beamed, observed brown dwarf quiescent emission likely originates from a magnetospheric population of electrons (Pineda et al. 2017; Kao et al. 2019; M. M. Kao & E. L. Shkolnik 2020, in preparation). We therefore expect that the velocity distribution of such a population of electrons will smear out the beaming from individual electrons. Measuring L and T dwarf inclination angles and incorporating the inclination angle dependence into a future study of radio emission on IR/variable L and T dwarfs will rule in or out geometric effects.

Additionally, we cannot rule out a connection between variability at longer IR wavelengths and radio emission. Quiescent radio emission correlates with markers of auroral activity in ultracool M, L, and T dwarfs (Pineda et al. 2017) that trace strong, kilogauss magnetic fields (Hallinan et al. 2008; Route & Wolszczan 2012; Kao et al. 2016, 2018) that may interact with the upper atmospheres of these objects (Hallinan et al. 2015; Pineda et al. 2017). Magnetic spot heating occurring near the top of the atmosphere may manifest as variability at longer wavelengths, with most flux differences occurring between 2–4 μm and 5–9 μm (Morley et al. 2014; Robinson & Marley 2014). While brown dwarf variability searches typically include the Spitzer IRAC channels 1 and 2 at 3.6 μm and 4.5 μm, respectively, targeted studies for photometric variability among all L dwarfs for which we see pulsed radio emission have searched only from 0.5 to 2.5 μm, probing the bottom layers of the bodies' atmospheres at 10 bar and higher (Robinson & Marley 2014).

Combining detections of radio aurorae implying strong magnetic fields and electron currents with studies at longer amplitudes will allow us to characterize if and how wavelength-dependent variability traces or rules out magnetic spot heating. Multi-wavelength studies of brown dwarfs with pulsed radio emission will be prime targets for James Webb Space Telescope's NIRCAM (0.6–5 μm) and MIRI (5.6–25.5 μm) instruments.

5.2. Auroral Tracers: Hα Emission or IR Variability?

For 2M1750-00, we observe a coherent ECM flare that is characterized by a broad peak in emission with additional substructure. Interestingly, 2M1750-00 additionally has measured Hα emission of $f_\alpha = (21.4 \pm 4.8) \times 10^{-18}$ erg s^{-1} cm^{-2} (Pineda et al. 2016). This was one of two objects in our sample for which Hα emission has been detected, with the caveat that several of the targets have not yet been observed for Hα emission. Pineda et al. (2017) demonstrated a tight correlation between Hα and quiescent radio luminosities among pulsed radio emitters (Pineda et al. 2017), and we show in Figure 5 that our detected target directly follows this relationship. If this relationship holds, then the other target in our sample with measured Hα emission, DENIS 1058-15, may be a good target for future follow-up observations.

Combining our results with those of Kao et al. (2016), we suggest that Hα in the spectra of a brown dwarfs regardless of its temperature points to non-thermal magnetic processes; furthermore, in late L- dwarfs and T dwarfs it is a reliable sign of auroral currents. This is unsurprising, since Hα has long been seen as an indicator of magnetic activity in the chromosphere of stars (e.g., Linsky et al. 1982; Walkowicz et al. 2008). Moreover, in the cooler atmospheres of brown dwarfs, Hα emission has been seen to decline rapidly (Berger et al. 2010; Williams et al. 2014; Schmidt et al. 2015), signaling the separation between stellar chromospheric magnetic activity and substellar magnetospheric activity. Pineda et al. (2016) found that the detection rate of Hα in brown dwarfs L4 and later was 9.2%, which is consistent with the the putative quiescent radio occurrence rate for L dwarfs (M. M. Kao & E. L. Shkolnik 2020, in preparation). Pineda et al. (2016) proposed that a possible connection between Hα emission and auroral activity could be through the raining down of electrons via flux tubes between a brown dwarf and an inferred satellite. Such a situation would mimic that of Io's auroral footprint on Jupiter (e.g., Vasavada et al. 1999). Therefore, it remains a possibility that there are yet undetected companions to brown dwarfs that exhibit Hα emission.

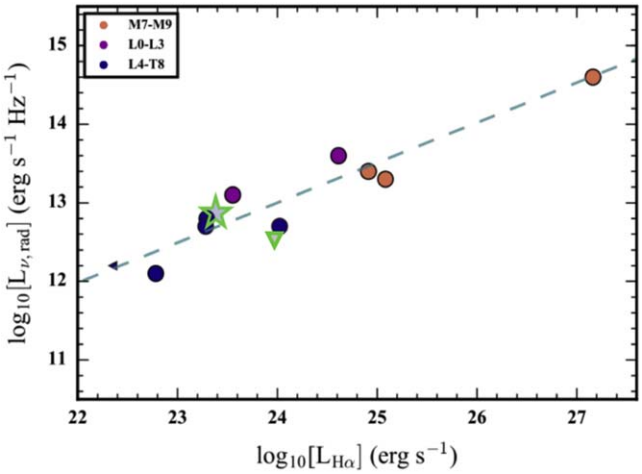

Figure 5. Hα luminosity compared to radio luminosity for pulsed radio emitters from Pineda et al. (2017). The addition of 2M1750-00 is represented by a green star and follows the known relationship well. DENIS 1058-15, the only other target with an Hα measurement, is also shown as a triangle representing the radio upper limit.

5.3. T Dwarf Aurorae and Photometric Variability

The results of this work will soon be combined with a similar study of the relationship between T Dwarf aurorae and O/IR variability to yield a complete picture throughout the range of brown dwarf spectral types through which radio aurorae have been observed (M. M. Kao et al. 2020, in preparation).

Because T dwarfs have different atmospheric compositions due to their cooler temperatures, the structure of the thermal profile and the ability for atmospheric circulation and transport may differ. Morley et al. (2014) showed that flux ratios from excess emission due to spot heating at various atmospheric depths both increases and shifts redward as objects cool from 1000 to 400 K. This suggests that magnetic spot heating may cause stronger photometric responses in T dwarfs.

6. Conclusions

We searched over 2 hr of observations for quiescent and/or pulsed radio emission in 17 L dwarfs from 4–8 GHz. We

observe highly circularly polarized, pulsed emission in only one target, 2M1750-00. Additionally, 2M1750-00 was the only object for which we observed quiescent radio emission, furthering the evidence that quiescent emission and auroral emission are related. We determine a lower limit on the magnetic field strength of 2M1750-00 of 2.9 kG.

We selected our sample for clear O/IR variability. Because we did not see a detection rate much greater than that of previous volume-limited samples, we infer that auroral magnetic activity does not play a role in the O/IR variability observed on these targets. The depth at which auroral magnetic activity may influence the atmosphere is not constrained, so observations at longer wavelengths that probe deeper into brown dwarf atmospheres may indeed show such a connection.

Our empirical results are supported by a theoretical framework to calculate the occurrence rate distributions of quiescent radio activity for brown dwarfs with low- and high-amplitude variability, based on the maximum-likelihood occurrence rate framework from M. M. Kao & E. L. Shkolnik (2020, in preparation). We find that the occurrence rates of quiescent emission in L dwarfs with low- and high-amplitude variability are between 5%–6% and 11%–26%, respectively, depending on the assumed cutoff between low- and high-amplitude variability. As we increased the amplitude cutoff from 1% to 3%, occurrence rate of the low-amplitude sample remained relatively constant, while the occurrence rate increased with increasing amplitude cutoff for the high-amplitude sample. However, we determine that this is an artifact of sample sizes and conclude that high-amplitude O/IR variability does not trace radio magnetic activity in L dwarfs. Future studies improving and expanding upon inclination measurements of brown dwarfs together with studies of IR variability beyond 5 μm will aid in forming a more thorough assessment of a relationship between brown dwarf photometric variability and radio magnetic activity.

Finally, we find that the only radio-bright object in our sample, 2M1750-00, is also an Hα emitter. We show that its quiescent radio luminosity is consistent with an existing correlation between Hα luminosities and quiescent radio luminosities in auroral ultracool dwarfs. We conclude that Hα emission in the spectra of brown dwarfs is the stronger indicator of strong magnetic fields traced by radio emission.

The authors would like to thank the anonymous referee for an insightful report. T.R.Y. and M.M.K. would like to thank Cameron Voloshin for consulting on the statistics of this study. T.R.Y. would additionally like to thank Danny Jacobs, Adam Beardsley, and Judd Bowman for useful discussions and CASA help. Support for this work was provided by NASA through the NASA Hubble Fellowship grant HST-HF2-51411.001-A awarded by the Space Telescope Science Institute, which is operated by the Association of Universities for Research in Astronomy, Inc., for NASA, under contract NAS5-26555; and by the National Radio Astronomy Observatory. The National Radio Astronomy Observatory is a facility of the National Science Foundation operated under cooperative agreement by Associated Universities, Inc. This work is based on observations made with the NSF's Karl G. Jansky Very Large Array (VLA). This research has made use of the SIMBAD and VizieR databases, operated at CDS, Strasbourg, France; and the European Space Agency (ESA) mission Gaia (https://www.cosmos.esa.int/gaia), processed by the Gaia Data Processing and Analysis Consortium (DPAC, https://www.cosmos.esa.int/web/gaia/dpac/consortium).

Software: CASA (McMullin et al. 2007), Astropy (Price-Whelan et al. 2018), Matplotlib (Hunter 2007), Numpy (van der Walt et al. 2011), Scipy (Jones et al. 2001), MATLAB (MATLAB 2018).

ORCID iDs

Tyler Richey-Yowell https://orcid.org/0000-0003-1290-3621
Melodie M. Kao https://orcid.org/0000-0001-5125-1414
J. Sebastian Pineda https://orcid.org/0000-0002-4489-0135
Evgenya L. Shkolnik https://orcid.org/0000-0002-7260-5821
Gregg Hallinan https://orcid.org/0000-0002-7083-4049

References

Allard, F., Hauschildt, P. H., Alexander, D. R., Tamanai, A., & Schweitzer, A. 2001, ApJ, 556, 357
Antonova, A., Doyle, J. G., Hallinan, G., Bourke, S., & Golden, A. 2008, A&A, 487, 317
Antonova, A., Hallinan, G., Doyle, J. G., et al. 2013, A&A, 549, A131
Apai, D., Radigan, J., Buenzli, E., et al. 2013, ApJ, 768, 121
Bailer-Jones, C. A. L., & Mundt, R. 1999, A&A, 348, 800
Bailer-Jones, C. A. L., & Mundt, R. 2001, A&A, 367, 218
Bardalez Gagliuffi, D. C., Burgasser, A. J., Gelino, C. R., et al. 2014, ApJ, 794, 143
Berger, E. 2002, ApJ, 572, 503
Berger, E. 2006, ApJ, 648, 629
Berger, E., Ball, S., Becker, K. M., et al. 2001, AAS Meeting Abstracts, 198, 69.06
Berger, E., Basri, G., Fleming, T. A., et al. 2010, ApJ, 709, 332
Berger, E., Rutledge, R. E., Reid, I. N., et al. 2005, ApJ, 627, 960
Biller, B. 2017, AstRv, 13, 1
Biller, B. A., Crossfield, I. J. M., Mancini, L., et al. 2013, ApJL, 778, L10
Blake, C. H., Bloom, J. S., Latham, D. W., et al. 2008, PASP, 120, 860
Bougher, S. W., Waite, J. H., Majeed, T., & Gladstone, G. R. 2005, JGRE, 110, E04008
Buenzli, E., Apai, D., Radigan, J., Reid, I. N., & Flateau, D. 2014, ApJ, 782, 77
Buenzli, E., Marley, M. S., Apai, D., et al. 2015a, ApJ, 812, 163
Buenzli, E., Saumon, D., Marley, M. S., et al. 2015b, ApJ, 798, 127
Burgasser, A. J., Cruz, K. L., Cushing, M., et al. 2010, ApJ, 710, 1142
Burgasser, A. J., Gillon, M., Faherty, J. K., et al. 2014, ApJ, 785, 48
Burgasser, A. J., Sheppard, S. S., & Luhman, K. L. 2013, ApJ, 772, 129
Caldwell, J., Tokunaga, A. T., & Gillett, F. C. 1980, Icar, 44, 667
Castro, P. J., Gizis, J. E., Harris, H. C., et al. 2013, ApJ, 776, 126
Chiu, K., Fan, X., Leggett, S. K., et al. 2006, AJ, 131, 2722
Clarke, F. J., Hodgkin, S. T., Oppenheimer, B. R., Robertson, J., & Haubois, X. 2008, MNRAS, 386, 2009
Clarke, F. J., Oppenheimer, B. R., & Tinney, C. G. 2002, MNRAS, 335, 1158
Clarke, F. J., Tinney, C. G., & Hodgkin, S. T. 2003, MNRAS, 341, 239
Clary, R. S., & Hunter, J. H. J. 1975, ApJ, 199, 517
Croll, B., Muirhead, P. S., Han, E., et al. 2016, arXiv:1609.03586
Cruz, K. L., Núñez, A., Burgasser, A. J., et al. 2018, AJ, 155, 34
Cruz, K. L., Reid, I. N., Liebert, J., Kirkpatrick, J. D., & Lowrance, P. J. 2003, AJ, 126, 2421
Drossart, P., Maillard, J. P., Caldwell, J., et al. 1989, Natur, 340, 539
Dupuy, T. J., & Liu, M. C. 2012, ApJS, 201, 19
Dupuy, T. J., & Liu, M. C. 2017, ApJS, 231, 15
Enoch, M. L., Brown, M. E., & Burgasser, A. J. 2003, AJ, 126, 1006
Faherty, J. K., Burgasser, A. J., Cruz, K. L., et al. 2009, AJ, 137, 1
Faherty, J. K., Burgasser, A. J., Walter, F. M., et al. 2012, ApJ, 752, 56
Faherty, J. K., Riedel, A. R., Cruz, K. L., et al. 2016, ApJS, 225, 10
Gagné, J., Faherty, J. K., Cruz, K. L., et al. 2015a, ApJS, 219, 33
Gagné, J., Lafrenière, D., Doyon, R., Malo, L., & Artigau, É 2015b, ApJ, 798, 73
Gaia Collaboration, Brown, A. G. A., Vallenari, A., et al. 2018, A&A, 616, A1
Gawroński, M. P., Goździewski, K., & Katarzyński, K. 2017, MNRAS, 466, 4211
Geballe, T. R., Jagod, M. F., & Oka, T. 1993, ApJL, 408, L109
Geballe, T. R., Knapp, G. R., Leggett, S. K., et al. 2002, ApJ, 564, 466

Gelino, C. R., Marley, M. S., Holtzman, J. A., Ackerman, A. S., & Lodders, K. 2002, ApJ, 577, 433
Gelino, C. R., Smart, R. L., Marocco, F., et al. 2014, AJ, 148, 6
Gillon, M., Triaud, A. H. M. J., Jehin, E., et al. 2013, A&A, 555, L5
Gizis, J. E., Williams, P. K. G., Burgasser, A. J., et al. 2016, AJ, 152, 123
Goldman, B., Cushing, M. C., Marley, M. S., et al. 2008, A&A, 487, 277
Guenther, E. W., Zapatero Osorio, M. R., Mehner, A., & Martín, E. L. 2009, A&A, 498, 281
Guirado, J. C., Azulay, R., Gauza, B., et al. 2018, A&A, 610, A23
Gurnett, D. A., Kurth, W. S., & Scarf, F. L. 1981, Natur, 292, 733
Hallinan, G., Antonova, A., Doyle, J. G., et al. 2006, ApJ, 653, 690
Hallinan, G., Antonova, A., Doyle, J. G., et al. 2008, ApJ, 684, 644
Hallinan, G., Bourke, S., Lane, C., et al. 2007, ApJL, 663, L25
Hallinan, G., Littlefair, S. P., Cotter, G., et al. 2015, Natur, 523, 568
Harding, L. K., Hallinan, G., Boyle, R. P., et al. 2013, ApJ, 779, 101
Heinze, A. N., Metchev, S., Apai, D., et al. 2013, ApJ, 767, 173
Heinze, A. N., Metchev, S., & Kellogg, K. 2015, ApJ, 801, 104
Hunter, J. D. 2007, CSE, 9, 90
Jackman, J. A. G., Wheatley, P. J., Bayliss, D., et al. 2019, MNRAS, 485, L136
Jameson, R. F., Casewell, S. L., Bannister, N. P., et al. 2008, MNRAS, 384, 1399
Jones, E., Oliphant, T., Peterson, P., et al. 2001, SciPy: Open Source Scientific Tools for Python, http://www.scipy.org/
Kao, M. M., Hallinan, G., Pineda, J. S., et al. 2016, ApJ, 818, 24
Kao, M. M., Hallinan, G., & Pineda, J. S. 2019, MNRAS, 487, 1994
Kao, M. M., Hallinan, G., Pineda, J. S., Stevenson, D., & Burgasser, A. 2018, ApJS, 237, 25
Kendall, T. R., Delfosse, X., Martín, E. L., & Forveille, T. 2004, A&A, 416, L17
Kendall, T. R., Jones, H. R. A., Pinfield, D. J., et al. 2007, MNRAS, 374, 445
Khandrika, H., Burgasser, A. J., Melis, C., et al. 2013, AJ, 145, 71
Kirkpatrick, J., Reid, I., Liebert, J., et al. 2000, AJ, 120, 447
Kirkpatrick, J. D., Cushing, M. C., Gelino, C. R., et al. 2011, ApJS, 197, 19
Kirkpatrick, J. D., Reid, I. N., Liebert, J., et al. 1999, ApJ, 519, 802
Koen, C. 2003, MNRAS, 346, 473
Koen, C. 2004, MNRAS, 354, 378
Koen, C. 2005, MNRAS, 360, 1132
Koen, C. 2013, MNRAS, 428, 2824
Koen, C., Matsunaga, N., & Menzies, J. 2004, MNRAS, 354, 466
Koen, C., Miszalski, B., Väisänen, P., & Koen, T. 2017, MNRAS, 465, 4723
Koen, C., Tanabé, T., Tamura, M., & Kusakabe, N. 2005, MNRAS, 362, 727
Krishnamurthi, A., Leto, G., & Linsky, J. L. 1999, AJ, 118, 1369
Lane, C., Hallinan, G., Zavala, R. T., et al. 2007, ApJL, 668, L163
Leggett, S. K., Allard, F., Geballe, T. R., Hauschildt, P. H., & Schweitzer, A. 2001, ApJ, 548, 908
Linsky, J. L., Bornmann, P. L., Carpenter, K. G., et al. 1982, ApJ, 260, 670
Littlefair, S. P., Dhillon, V. S., Marsh, T. R., Shahbaz, T., & Martín, E. L. 2006, MNRAS, 370, 1208
Liu, M. C., Dupuy, T. J., & Allers, K. N. 2016, ApJ, 833, 96
Looper, D. L., Kirkpatrick, J. D., Cutri, R. M., et al. 2008, ApJ, 686, 528
Lunine, J. I., Hubbard, W. B., Burrows, A., Wang, Y.-P., & Garlow, K. 1989, ApJ, 338, 314
Lynch, C., Murphy, T., Ravi, V., et al. 2016, MNRAS, 457, 1224
Maiti, M. 2007, AJ, 133, 1633
MATLAB 2018, version R2018b (Natick, MA: The MathWorks Inc.)
McLean, M., Berger, E., & Reiners, A. 2012, ApJ, 746, 23
McMullin, J. P., Waters, B., Schiebel, D., Young, W., & Golap, K. 2007, in ASP Conf. Ser. 376, CASA Architecture and Applications, ed. R. A. Shaw, F. Hill, & D. J. Bell (San Francisco, CA: ASP), 127
Melrose, D. B., Hewitt, R. G., & Dulk, G. A. 1984, JGR, 89, 897
Metchev, S. A., Heinze, A., Apai, D., et al. 2015, ApJ, 799, 154
Miles-Páez, P. A., Metchev, S. A., Heinze, A., & Apai, D. 2017, ApJ, 840, 83
Mohanty, S., Basri, G., Shu, F., Allard, F., & Chabrier, G. 2002, ApJ, 571, 469
Morley, C. V., Marley, M. S., Fortney, J. J., & Lupu, R. 2014, ApJL, 789, L14
Nakajima, T., Oppenheimer, B. R., Kulkarni, S. R., et al. 1995, Natur, 378, 463
Osten, R. A., & Bastian, T. S. 2006, ApJ, 637, 1016
Osten, R. A., Melis, C., Stelzer, B., et al. 2015, ApJL, 805, L3
Paudel, R. R., Gizis, J. E., Mullan, D. J., et al. 2018, ApJ, 858, 55
Paudel, R. R., Gizis, J. E., Mullan, D. J., et al. 2020, MNRAS, 494, 5751
Phan-Bao, N., Bessell, M. S., Martín, E. L., et al. 2008, MNRAS, 383, 831
Pineda, J. S., & Hallinan, G. 2018, ApJ, 866, 155
Pineda, J. S., Hallinan, G., & Kao, M. M. 2017, ApJ, 846, 75
Pineda, J. S., Hallinan, G., Kirkpatrick, J. D., et al. 2016, ApJ, 826, 73
Pottelette, R., Ergun, R. E., Treumann, R. A., et al. 1999, GeoRL, 26, 2629
Price-Whelan, A. M., Sipócz, B. M., Günther, H. M., et al. 2018, AJ, 156, 123
Radigan, J. 2014, ApJ, 797, 120
Radigan, J., Lafrenière, D., Jayawardhana, R., & Artigau, E. 2014, ApJ, 793, 75
Radigan, J. M. 2013, PhD thesis, Univ. Toronto, Canada
Reid, I. N., Cruz, K. L., Kirkpatrick, J. D., et al. 2008, AJ, 136, 1290
Reid, I. N., Kirkpatrick, J. D., Gizis, J. E., et al. 2000, AJ, 119, 369
Reid, I. N., Lewitus, E., Allen, P. R., Cruz, K. L., & Burgasser, A. J. 2006, AJ, 132, 891
Reiners, A., & Basri, G. 2008, ApJ, 684, 1390
Robinson, T. D., & Marley, M. S. 2014, ApJ, 785, 158
Route, M., & Wolszczan, A. 2012, ApJL, 747, L22
Route, M., & Wolszczan, A. 2013, ApJ, 773, 18
Route, M., & Wolszczan, A. 2016, ApJ, 830, 85
Salim, S., Lépine, S., Rich, R. M., & Shara, M. M. 2003, ApJL, 586, L149
Schlawin, E., Burgasser, A. J., Karalidi, T., Gizis, J. E., & Teske, J. 2017, ApJ, 849, 163
Schmidt, S. J., Cruz, K. L., Bongiorno, B. J., Liebert, J., & Reid, I. N. 2007, AJ, 133, 2258
Schmidt, S. J., Hawley, S. L., West, A. A., et al. 2015, AJ, 149, 158
Schmidt, S. J., Shappee, B. J., Gagné, J., et al. 2016, ApJL, 828, L22
Schmidt, S. J., West, A. A., Hawley, S. L., & Pineda, J. S. 2010, AJ, 139, 1808
Schneider, A. C., Cushing, M. C., Kirkpatrick, J. D., et al. 2014, AJ, 147, 34
Scholz, R. D., & Meusinger, H. 2002, MNRAS, 336, L49
Siegler, N., Close, L. M., Burgasser, A. J., et al. 2007, AJ, 133, 2320
Sinclair, J. A., Orton, G. S., Fernandes, J., et al. 2019, NatAs, 3, 607
Skrutskie, M. F., Cutri, R. M., Stiening, R., et al. 2006, AJ, 131, 1163
Smart, R. L., Tinney, C. G., Bucciarelli, B., et al. 2013, MNRAS, 433, 2054
Stumpf, M. B., Brandner, W., Bouy, H., Henning, T., & Hippler, S. 2010, A&A, 516, A37
Tinney, C. G., Delfosse, X., & Forveille, T. 1997, ApJL, 490, L95
Trafton, L. M., Geballe, T. R., Miller, S., Tennyson, J., & Ballester, G. E. 1993, ApJ, 405, 761
Tremblin, P., Amundsen, D. S., Chabrier, G., et al. 2016, ApJL, 817, L19
Tremblin, P., Amundsen, D. S., Mourier, P., et al. 2015, ApJL, 804, L17
Treumann, R. A. 2006, A&ARv, 13, 229
Tsuji, T. 2002, ApJ, 575, 264
van der Walt, S., Colbert, S. C., & Varoquaux, G. 2011, CSE, 13, 22
Vasavada, A. R., Bouchez, A. H., Ingersoll, A. P., et al. 1999, JGR, 104, 27133
Villadsen, J., & Hallinan, G. 2019, ApJ, 871, 214
Vos, J. M., Allers, K. N., & Biller, B. A. 2017, ApJ, 842, 78
Vos, J. M., Allers, K. N., Biller, B. A., et al. 2018, MNRAS, 474, 1041
Vos, J. M., Biller, B. A., Allers, K. N., et al. 2020, AJ, 160, 38
Vos, J. M., Biller, B. A., Bonavita, M., et al. 2019, MNRAS, 483, 480
Walkowicz, L. M., Johns-Krull, C. M., & Hawley, S. L. 2008, ApJ, 677, 593
Williams, P. K. G., & Berger, E. 2015, ApJ, 808, 189
Williams, P. K. G., Casewell, S. L., Stark, C. R., et al. 2015, ApJ, 815, 64
Williams, P. K. G., Cook, B. A., & Berger, E. 2014, ApJ, 785, 9
Wilson, P. A., Rajan, A., & Patience, J. 2014, A&A, 566, A111
Yang, H., Apai, D., Marley, M. S., et al. 2015, ApJL, 798, L13
York, D. G., Adelman, J., Anderson, J. E., Jr., et al. 2000, AJ, 120, 1579
Zarka, P. 1992, AdSpR, 12, 99